Snow accumulation patterns from 2023 Airborne Laser Scanning data in Trail Valley Creek, Western Canadian Arctic

Daniela Hollenbach Borges

Supervisors:

Prof. Dr. Julia Boike

Dr. Inge Grünberg

A thesis presented for the degree of
Master of Science

Department of Geography
Humboldt-Universität zu Berlin
Germany

January 23, 2025

Snow accumulation patterns from 2023 Airborne Laser Scanning data in Trail Valley Creek, Western Canadian Arctic

Abstract

Trail Valley Creek, located in the Northwest Territories (NWT), approximately 45 km north of Inuvik, Canada, marks the northern boundary of the tundra-taiga transition zone. This region, underlain by continuous permafrost, is experiencing rapid warming and vegetation changes, including shrub expansion. These shifts may lead to increased snow depths, which could in turn affect subsurface temperatures and potentially impact permafrost stability.

Topography and vegetation are key drivers of spatial variation in snow depth, with wind redistribution leading to snow accumulation in topographic lows, leeward slopes, and densely vegetated areas. However, landscape complexity also affects snow measurement accuracy, adding variability to depth estimates. Understanding these relationships is essential but often limited by the scarcity of high-resolution, large-scale data that can capture landscape heterogeneity. In this study, I investigated snow depth patterns across different topographic features (landforms, slopes, and aspects) and vegetation types (height ranges and cover classes) within an area of 127 km^2. To achieve this, I used LiDAR (Light Detection and Ranging) data collected over the snow-covered surface (April 2, 2023) and the snow-free terrain (July 10, 2023) of Trail Valley Creek to create a 1-meter resolution snow depth map. I then compared the LiDAR data with two reference sources: 9569 coordinate reference points along the Inuvik-Tuktoyaktuk Highway (ITH), which intersects the area and is maintained at minimal snow depth throughout winter, and snow depth measurements from 4615 field survey points. Field surveys recorded deeper snow depths than LiDAR estimates, with an overall bias of 0.18 m. The discrepancy between LiDAR and field measurements varied significantly, with the largest biases over trees (0.30 m) and on steep east-facing slopes (0.37 m). However, LiDAR measurements closely aligned with the ITH reference points, showing a median depth deviation of just 0.017 m. The analysis showed that, with regard to topography, snow depth was highest over footslopes and valleys, with median depths of 0.38 m and 0.44 m, respectively, and lowest on ridges (0.20 m). Snow depth also increased with slope steepness and was consistently greater on east-facing slopes, in response to predominant winds from the west and northwest. In terms of vegetation, snow depth increased with vegetation height, with medians ranging from 0.29 m over vegetation shorter than 0.50 m to 0.54 m in areas where vegetation height exceeded 1.5 m. These findings align with results by vegetation class, where single and riparian shrubs exhibited the highest accumulations, with snow depth medians reaching 0.49 m.

Contents

List of Figures

List of Tables

Introduction

The Arctic air temperatures have risen at least twice as fast as the global averages in the past decades (Biskaborn et al., 2019; Langer et al., 2023; Taylor et al., 2013). As a consequence of the rapid warming, the overall snow cover duration is likely reduced, with later snow fall begin in autumn and earlier snow melt in spring (IPCC, 2022), impacting Arctic ecosystems and landscapes. Permafrost is particularly sensitive to climatic variations such as increases in air and ground temperatures and changes in snow regimes (Biskaborn et al., 2019). The shorter snow cover seasons are likely to reduce species richness and accelerate local extinctions (Niittynen et al., 2018).

1.1 Permafrost and snow cover

Permafrost is defined as ground that remains frozen for two or more consecutive years (Harris et al., 1988). Its warming and thawing has the potential to amplify global climate change through the release of methane and carbon dioxide from permafrost into the atmosphere (Chadburn et al., 2017; Schuur et al., 2015). Permafrost thaw also impacts ecosystems, hydrological systems (Biskaborn et al., 2019), and can be damaging to civil infrastructures and industrial plants above and below ground, potentially leading to the release of toxic chemicals such as hydrocarbons and heavy metals into soil, surface and ground water (Langer et al., 2023; Schneider von Deimling et al., 2021). Permafrost is also highly influenced by seasonal snow covers, as snow depth variations affect the biogeochemical properties (Zhao et al., 2022) and the temperature variability in upper soil layers (Callaghan et al., 2011b; Zhang, 2005).

Snow has low thermal conductivity properties, and insulates the ground surface from the atmosphere, actively protecting the ground from substantial energy loss in winter (Callaghan et al., 2011a). Thin snow layers, with reduced insulating capacity yet high albedo, tend to cool the ground surface temperatures during winter (Zhao et al., 2022). On the other hand, increased snow depth enhances the insulation effect, leading to warmer soil temperatures (Zhang, 2005), increasing soil moisture (Zhao et al., 2022), and favoring organic matter decomposition (Walker et al., 2001). Snow cover, therefore, plays a critical role in the energy and moisture fluxes, and consequently in the formation and development of seasonally frozen ground and permafrost (Callaghan et al., 2011b; Gouttevin et al., 2012). The accumulation of thicker snow layers, facilitated by the trapping effect of shrubs and surface microrelief, contributes to an increase in soil temperatures, which in turn accelerates permafrost thawing (Zhang, 2005).

Snow depth variations are mainly driven by topography and vegetation (Pohl and Marsh, 2006; Walker et al., 2020), which serve as natural structures that facilitate snow accumulation and retention (Derksen et al., 2009; Sturm et al., 2001). Terrain features such as valleys and microtopographic lows (Wainwright et al., 2017), along with taller vegetation such as shrubs and trees (Pohl and Marsh, 2006; Thompson et al., 2016), significantly contribute to intercepting snow in Arctic landscapes.

In the short term, understanding snow depth distribution is crucial for the estimation of snow water equivalent and therefore the prediction of water availability (Hopkinson et al., 2012) and risk of flooding (Hopkinson et al., 2004). In the long term, the northward expansion of shrub cover, a well-documented ongoing phenomenon associated with climate change (Beamish et al., 2020; Sturm et al., 2001), is likely to promote the increase of snow depths by 10-25% (Sturm et al., 2001). This underscores the importance of comprehending the unfolding changes in snow cover and their impact on permafrost dynamics.

1.2 Snow assessment techniques

Several methodologies have been used to observe and retrieve snow features and snow depth information, ranging from broad-scale satellite observations to high-resolution remote sensing techniques and localized field measurements.

Optical satellite data provide valuable information on snow cover extent (Harder et al., 2016), as snow exhibits distinct spectral characteristics in the visible and middle-infrared wavelengths, creating a clear contrast with other natural surfaces (Wu et al., 2021). However, satellite imagery is highly impacted by the lack of sunlight and the presence of cloud cover (Aalstad et al., 2020). The temporal resolution often does not align with the rapid changes in the snow line during spring melt (Derksen et al., 2009), and the spatial resolution not always accomplish to capture the complexities of the snow's spatial variability (Callaghan et al., 2011a; Harder et al., 2016; Hopkinson et al., 2008). Satellite microwave sensors such as the Advanced Microwave Scanning Radiometer (AMSR) series, the Special Sensor Microwave/Imager (SSM/I) and Synthetic Aperture Radar (SAR), on the other hand, operate at longer wavelengths and are able to retrieve surface information regardless the presence of sunlight and cloud cover. Passive microwave remote sensing has traditionally been used in the estimation of snow water equivalent (Derksen et al., 2009; Rutter et al., 2019).

However, the coarse spatial resolution of satellite data is not optimal to capture the variability in the physical properties of snow (Derksen et al., 2009; Rutter et al., 2014) and its seasonal microstructural evolution (Rutter et al., 2019). While satellite data remain indispensable for large-scale monitoring and assessment of remote Arctic landscapes (Beamish et al., 2020), such as through the extensive time series provided by platforms like Landsat, which have been instrumental in revealing long-term changes in vegetation cover and biomass (Berner et al., 2020; Nill et al., 2022) there are significant limitations. Snow depth can significantly vary across short distances driven by microtopographic variations, making it essential to obtain data at finer geographical scales. The impact of snow depth in hydrology and ecosystem functioning demands the knowledge of a broad regional context but also detailed local assessments (Wainwright et al., 2017). To address this, direct approaches, such as field snow depth measurements, ground and airborne high-resolution remote sensing tools like Ground Penetrating Radar (GPR), Structure from Motion (SfM), and Light Detection and Ranging (LiDAR), provide alternatives for capturing fine-scale snow variability and supporting both regional and local analyses (Dharmadasa et al., 2022; Wainwright et al., 2017).

GPR, extensively used for snow on sea ice (Wang, Wei, 2022) and estimations of snow water equivalent, use radio waves and microwaves to characterize snow depth, stratigraphy, density and by detecting variations in the dielectric properties throughout the snow pack (Wainwright et al., 2017; Wang, Wei, 2022). The radar equipment can be transported by foot, snow mobile (Derksen et al., 2009; Rutter et al., 2019), or from airborne platforms (Krumpen et al., 2023). However, the snow depth estimation with the use of radar can be influenced by terrain complexities such as steep slopes, hummocks (Painter et al., 2016; Wang, Wei, 2022), and ice-wedge polygons, due to radar positioning and ray path assumptions (Wainwright et al., 2017). Additionally, retrieving snow depth in vegetated areas, particularly where vegetation protrudes through the snowpack, presents challenges. Vegetation increases the complexity of radar signals, as it interacts with the waveform before and after it is attenuated by snow (Painter et al., 2016; Wang, Wei, 2022).

SfM is a technique that utilizes photogrammetry to produce high-resolution digital elevation models. By capturing multiple images from various angles, a software identifies and matches common surface tie points to align and aggregate the photos into a 3-dimensional representation of the surface (Nadal-Romero et al., 2015; Walker et al., 2020). This method is used to generate snow depth products and can be deployed using both manned and unmanned aerial vehicles (UAVs). UAVs, in particular, have become a viable alternative for small-scale, high-resolution remote sensing applications, offering a lower cost of operation compared to other methods such as LiDAR (Harder et al., 2016). While UAVs offer a flexible and cost-effective approach for SfM-based snow depth measurement, the method is not without challenges. Lighting conditions, for example, can highly affect the accuracy and quality of SfM snow depth products (Revuelto et al., 2021), particularly in polar regions where short daylight periods restrict data collection windows. Additionally, high wind speeds can shorten UAV and camera battery life, and cold temperatures can compromise equipment performance (Walker et al., 2020).

LiDAR is an active remote sensing technology (Hopkinson et al., 2008) that has become an indispensable tool in cryospheric studies due to its ability to produce dense, high-quality point clouds that detect snow cover and under-canopy ground points (Dharmadasa et al., 2022). LiDAR operates by emitting laser pulses that reflect back to the emitting sensor upon reaching a target surface. The system calculates the distance from the sensor to the target for each pulse, and by integrating multiple georeferenced pulses, it generates a point cloud of elevation measurements (Painter et al., 2016). LiDAR sensors can be deployed in various ways, including on tripods or stationary platforms in terrestrial laser scanning (TLS), a technique widely used in geology and forestry (Nadal-Romero et al., 2015). They can also be mounted on UAVs for small-scale, high-resolution mapping (Dharmadasa et al., 2022), or on aircraft, where the method is known as airborne laser scanning (ALS) (Hopkinson et al., 2008; Krumpen et al., 2023; Lange et al., 2021). Nevertheless, LiDAR measurements can encounter certain challenges and be influenced by positional errors, particularly in complex and steep terrains (Dharmadasa et al., 2022). Furthermore, dense vegetation can intercept a portion of the laser pulses, resulting in a less dense point cloud at ground level (Hopkinson et al., 2004), which may result in a systematic underestimation of snow depth in areas with dense understory (Hopkinson et al., 2008). Post-processing errors can also cause the misclassification of terrain features, such as ground points classified as non-ground points and the reverse (Dharmadasa et al., 2022; Pingel et al., 2013).

In cryospheric applications, snow depths are typically determined by differencing elevation models from snow-covered and snow-free periods (Dharmadasa et al., 2022; Hopkinson et al., 2004; Painter et al., 2016). This can be achieved using the same method for both models, such as LiDAR, as demonstrated in studies by Painter et al. (2016), King et al. (2018), Rutter et al. (2019), Dharmadasa et al. (2022), and Hammar et al. (2023). Dai et al. (2024) also applied a similar approach using ArcticDEM, derived from Maxar satellite stereoscopic imagery, to generate both snow-covered and snow-free elevation models. The snow-covered DEMs were created from winter acquisitions, while the snow-free DEMs were based on the median of summer ArcticDEM datasets of the same area. Alternatively, different methods can also be combined to derive snow depth, as seen in Walker et al. (2020), who used a snow-covered elevation model derived from SfM alongside a bareground LiDAR digital elevation model from Hopkinson et al. (2008). Similarly, Parr et al. (2020) averaged and fused a LiDAR and an SfM snow-free digital elevation model to base their snow depth calculations.

While geophysical methods provide valuable insights into snowpack properties, field measurements remain an essential approach for obtaining direct and ground-truth data on snow depth (Wainwright et al., 2017). Traditional field techniques, such as snow depth probing, are fundamental for both measuring snow depth and validating remote sensing products (Deems et al., 2013). This method involves the insertion of a cylindrical probe into the snowpack to measure the distance between the snow surface and the ground (Sturm and Holmgren, 2018). Despite their directness and reliability, field measurements have their own limitations. Probes can sometimes overestimate snow depth when they penetrate soft ground beneath the snowpack, introducing potential bias in the data (Berezovskaya and Kane, 2007). Additionally, positioning uncertainties can range from 3 m (Sturm and Holmgren, 2018) to 10 m, depending on the accuracy of the positioning system used (Walker et al., 2020). Furthermore, although field measurements provide direct data, they can be labor-intensive (Hopkinson et al., 2004) and may not capture the full spatial variability of snow depth across heterogeneous landscapes (Deems et al., 2013).

1.3 Study area

Trail Valley Creek is located in the Northwest Territories, Canada, within the transition zone between the northern edge of the boreal forest and the southern edge of the Arctic shrub tundra (Figure 1.1). The area is underlain by continuous permafrost, with a thickness ranging from 100 to 150 m (Marsh et al., 2008). The region is characterized by lakes, gently rolling hills and lowlands, with fairly low relief and deeply incised valleys (Pohl and Marsh, 2006). The upland areas are characterized by low tundra vegetation, while shrub tundra and sparse black spruce are found in valleys and adjacent hillslopes (Grünberg et al., 2020; Pohl and Marsh, 2006). Trail Valley Creek has a low Arctic climate, characterized by short and cool summers and long cold winters (Pomeroy et al., 1997; Walker et al., 2020), and is covered by snow 8 months a year, from October to May, being snow responsible for half of the annual precipitation (Pan et al., 2016).

In November 2017, the ITH opened, connecting Inuvik to Canada's Arctic coast. Running south to north along the western edge of Trail Valley Creek, this all-weather road, built on permafrost, has since influenced snow depth patterns along its route (Hammar et al., 2023).

The Trail Valley Creek research station (68.7420, -133.4992) began operations in 1991 (AHRG), and since the 1990's, researchers investigate the relationship between snow accumulation patterns and landscape features in the area. For instance, Pomeroy et al. (1997) demonstrated that landscape patterns, rather than just winter precipitation, significantly influence snow accumulation and loss. Subsequently, Essery and Pomeroy (2004) investigated the influence of shrubs on blowing snow fluxes, while Pohl and Marsh (2006) and (Marsh et al., 2008) simulated snow accumulation and melt in the tundra. The Alfred Wegener Institute, Helmholtz Centre for Polar and Marine Research (AWI) conducted its first airborne survey campaign at Trail Valley Creek in the summer of 2016 (Anders et al., 2018), and since then, further surveys have been carried out in the summer 2018 (Lange et al., 2021), winter 2019 (Hammar et al., 2023), and winter (Krumpen et al., 2023) and summer 2023 (Perma-X Crew, 2023). The research aircraft for these campaigns were equipped with a Modular Aerial Camera System (MACS), radar, and LiDAR sensor (Krumpen et al., 2023).

Digital elevation models created from the LiDAR data have enabled the investigation of bare ground and snow-covered terrain, as well as canopy height. This has advanced research on vegetation cover (Grünberg and Boike, 2019; Grünberg et al., 2020), vegetation height (Antonova et al., 2019), snow depth patterns (Hammar et al., 2023; Wang, Wei, 2022), and also served as a benchmark for other digital elevation models (Dai et al., 2024).

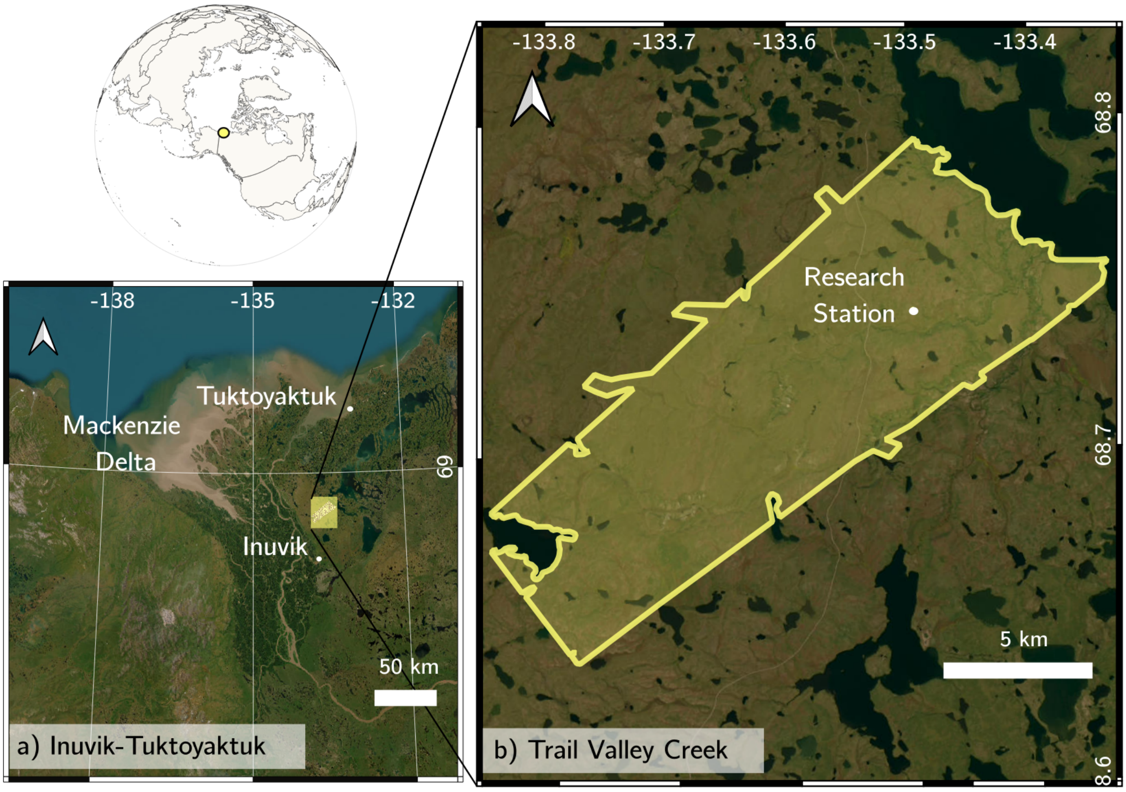

Figure 1.1: Trail Valley Creek and area of interest. a) Region of Trail Valley Creek, located $45\,\mathrm{km}$ north from Inuvik and $70\,\mathrm{km}$ south from the Arctic ocean in Northwest Territories, Canada. b) Area of interest (in yellow), in the surrounding area of the Trail Valley Creek Research Station.

1.4 Research focus and scope

Snow depth distribution in the Arctic is largely influenced by landscape features such as topography and vegetation. However, complex and densely vegetated terrains increase the uncertainty in digital elevation models, adding challenges to accurate snow depth measurements. In this study, I investigate the geomorphology, slope and aspect, vegetation height and cover, and their links with snow depth distribution in the area of Trail Valley Creek. Using high-resolution winter and summer digital elevation models along with in-situ snow depth measurements, the research is structured around three core questions:

RQ1 How do LiDAR snow depth measurements compare with control points over the ITH, and to field snow depth surveys?

RQ2 What is the LiDAR snow depth distribution across different geomorphological, topographical, and exposure settings in Trail Valley Creek, and how do field snow depth surveys compare within these classifications?

RQ3 What is the LiDAR snow depth distribution across different vegetation height and vegetation classes in Trail Valley Creek, and how do field snow depth surveys align with these classifications?

The first research question focuses on how LiDAR snow depth measurements compare with control points along the ITH, as well as how LiDAR data relates to field snow depth surveys. I hypothesize that LiDAR snow depths along the midpoint coordinates of the ITH will approximate zero, as the road is expected to have little to no snow cover. I also expect field snow depth measurements to be higher than those obtained from LiDAR, due to potential overestimation caused by snow probes and the tendency of LiDAR to underestimate snow depth, particularly in vegetated areas. The objective for this research question is twofold: first, to validate the accuracy of LiDAR snow depth measurements by comparing them to control points on the ITH; second, to assess the relationship between LiDAR and field measurements by comparing the results from both techniques.

The second research question examines how snow depth distribution varies across different geomorphological, topographical, and exposure settings in Trail Valley Creek. I hypothesize that topographical lows, such as valleys and footslopes, will accumulate more snow compared to ridges and plateaus. I also expect snow distribution to vary by exposure, with wind transportation and erosion leading to non-uniform snow depths across slopes and aspects. Moreover, I anticipate that the bias between LiDAR and field measurements will vary depending on the topographical context. The objective of this research is to quantify snow depth variation across geomorphological features and assess how topographical factors, including slope and aspect, influence snow depth patterns.

The third research question focuses on the role of vegetation in snow depth distribution across different vegetation heights and classes in Trail Valley Creek. I hypothesize that taller vegetation, such as shrubs and trees, will be associated with deeper snow depths, while the bias between LiDAR and field snow depth measurements will increase with vegetation height and density. The objective of this research is to quantify snow depth variation across different vegetation types and to analyze how vegetation height and class impact snow accumulation, offering insights into the relationship between vegetation and snow distribution.

Datasets and methods

To investigate the snow depth distribution in Trail Valley Creek, this study employed LiDAR snow depth data from 2023. The methodology was structured to address three key aspects: validating LiDAR measurements against control points along the ITH and field measurements, analyzing snow depth across various topographical settings such as landforms, slope and aspect, and examining the influence of different vegetation covers and heights.

I used LiDAR data acquired in the winter of 2023 (Krumpen et al., 2023) to create the snow-covered digital surface model (DSM). The summer 2023 LiDAR survey (Perma-X Crew, 2023) provided the base for the vegetation height map, and the digital terrain models (DTMs), which I used to generate landform, slope, and aspect maps. By subtracting the summer DTM from the winter DSM, I produced the snow depth map. The vegetation class map was sourced from the summer 2018 LiDAR campaign (Lange et al., 2021). To delineate the ITH midpoint, I used the ESRI Satellite basemap as a reference (Esri et al., 2023). Additionally, I utilized field survey datasets collected in the winter of 2023 by Rutter (2023) and Walker (2023). All rasters, the ones I used as a source and the ones I produced for this work, are saved as GeoTIFF files with a 1-meter resolution per pixel. The effective common area of interest totals 127.7 km^2. The following sections detail each of those steps, the workflow (Figure 2.1) and methodology employed in this research.

2.1 Mapping snow depth

2.1.1 DSM generation from snow covered terrain

Data source background: IceBird Winter 2023 campaign

I generated the snow-covered DSM using LiDAR point cloud data generated during the 2023 Winter campaign of the IceBird program, a long-term airborne Arctic sea ice and snow cover observation initiative led by AWI. The coinciding with the minimum sea-ice extent in August and the maximum in March and April (AWI, 2024c). The program aims to improve understanding of Arctic changes by collecting high-resolution data, quantifying trends, and validating sea-ice and snow depth estimates from products such as CryoSat-2, ICESat-2, and Sentinel-3A/B (Krumpen et al., 2023).

The 2023 campaign, conducted aboard the research aircraft Polar 6, was equipped

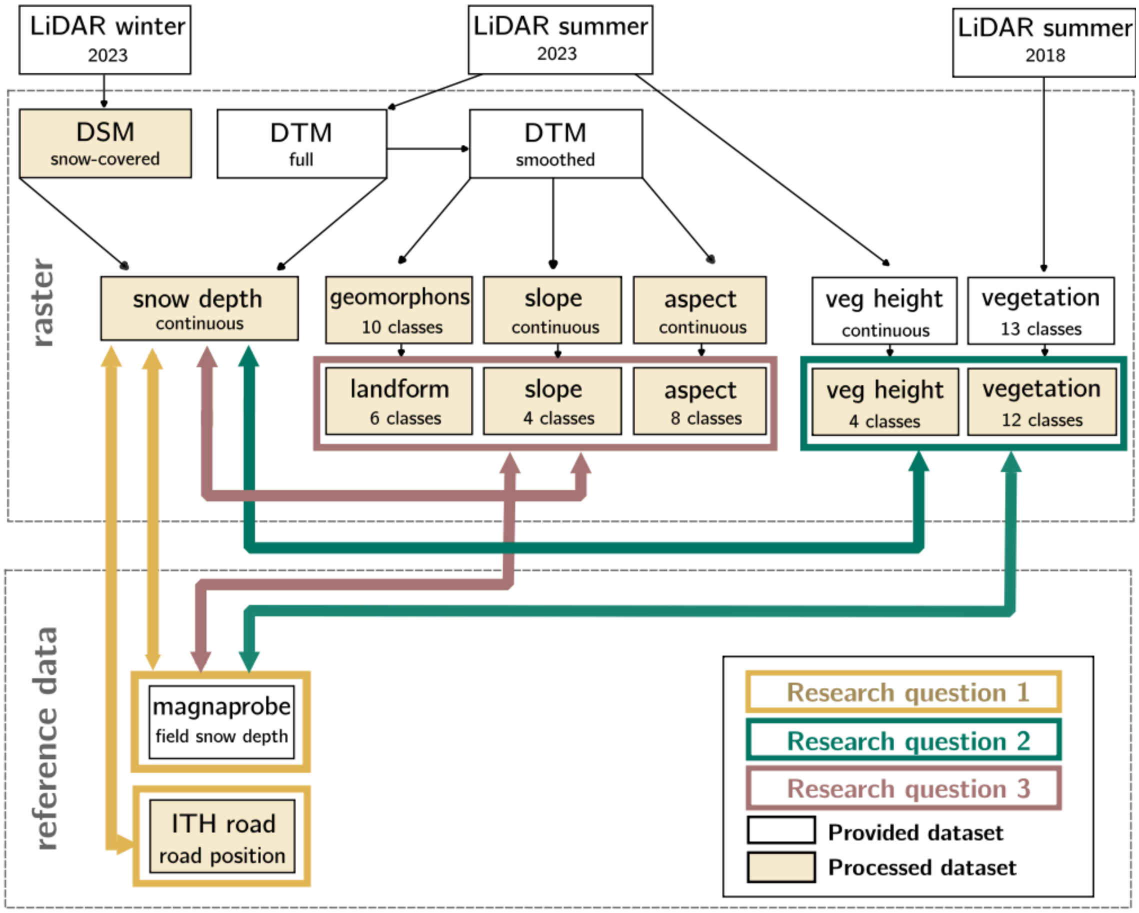

Figure 2.1: Datasets and workflow: The diagram illustrates this thesis' workflow. The yellow arrows indicate the comparison of LiDAR snow depths with reference field survey data (Rutter, 2023; Walker, 2023) and reference coordinates over the ITH. The brown and green arrows indicate the snow distribution analysis across topography and vegetation features, respectively. All the datasets in white boxes were processed outside this thesis and have been kindly provided for this work, and the datasets processed for this research are displayed in the beige boxes.

with the Airborne Electromagnetic (AEM) Bird—a sensor that detects the ice-water interface by contrasting the electrical conductivity of sea water and sea ice—as well as a Modular Aerial Camera System (MACS), snow radar, radiation sensors, and a LiDAR system, which provided the data for the snow-covered DSM.

The Polar 6 survey over Trail Valley Creek, organized by Julia Boike and Inge Grünberg, took place on April 2, 2023. This survey deployed LiDAR sensors, snow radar, and optical cameras (Table 2.1). The survey covered the area of interest in 15 rounds, each following a looped trajectory. These loops consisted of 26 parallel flight lines oriented from northeast to southwest, supplemented by additional lines running west to east, north to south, and intersecting the parallel paths from northwest to southeast, as illustrated in Figure 2.2.

LiDAR can be deployed from various platforms (Nadal-Romero et al., 2015), including aircraft, drones, and ground-based systems. In ALS, LiDAR operates by emitting laser pulses from an aircraft toward the ground and measuring the time it takes for each pulse to return after hitting a surface. Knowing the flight height and

Table 2.1: Flight and equipment configuration

Parameter	Specification
Flight altitude	1800 ft (550 m) a.s.l.
LiDAR settings	Frequency: 200 kHz, point spacing: 0.7m, point density: 2 pts/m^{3*}
Weather conditions	Temperature: -20° C, partly cloudy (high ceiling)

*Total point density considering overlap = 6 pts/m^3.

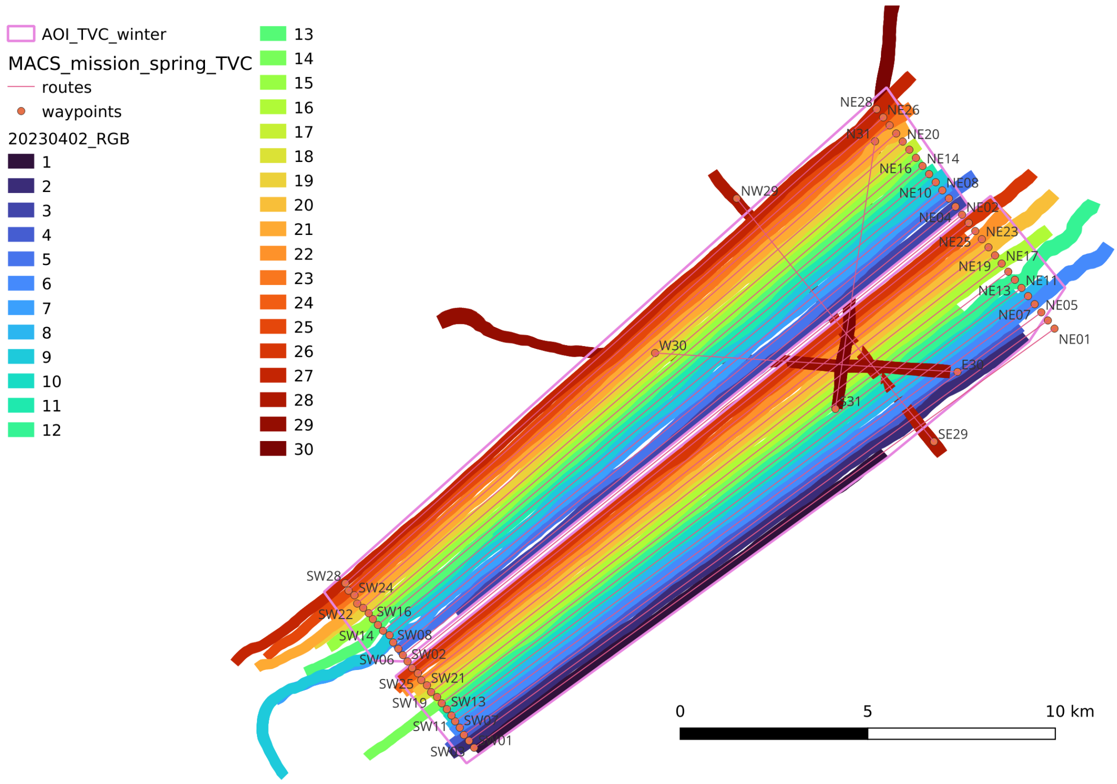

Figure 2.2: Flight plan outline: Polar-6 flight path original plan over Trail Valley Creek in the Winter 2023 expedition (Krumpen et al., 2023)

speed allows conversion of this travel time into a distance measurement (Painter et al., 2016). These sensors generate data that is converted into point clouds, with x, y, and z coordinates recorded for each point, and used to create a digital surface model. For the ICEBird 2023 winter campaign, the LiDAR survey used the Riegl VQ-580 airborne laser scanner, specifically designed for snow and ice measurements (RIEGL, 2015). Details of its configuration are provided in Table 2.2.

Pre-processing

The LiDAR survey data was processed at AWI by Veit Helm into 15 Level 1 (L1) point clouds, each corresponding to a flight loop. L1 processing involves initial data calibration, from the sensor's raw data to georeferenced, noise-reduced, point clouds. I then followed the workflow from Hammar et al. (2023), who processed

Table 2.2: Riegl VQ-580 technical specifications

Parameter	**Value**
Field of view	+/- 30°
Angle measurement resolution	0.001°
Scan speed (selectable)	10 – 150 lines per second
Laser pulse repetition rate (selectable)	50 – 380 kHz
Minimum range	10 m
Accuracy	25 mm
Precision	25 mm
Wavelength	near infrared (1064 nm)
Laser class	3B

the IceBird Winter 2019 expedition's raw LiDAR data to similarly generate a snow-covered DSM and subsequently a snow depth map. The processing steps were done in Python 3.12, as outlined below:

Reprojection: To prepare for indexing the point clouds with the LAStools Software Suite (Isenburg, 2023), I reprojected the point clouds from WGS 84 EPSG 4326 to UTM zone 8 EPSG 26908. LAStools, which includes over 50 open-source and licensed command-line tools for LiDAR processing, requires this reprojection because it does not process negative coordinates.

Indexing: After reprojecting the files, I indexed them using the open-source tool 'lasindex" from LAStools. This tool generates a LAX index file in the same directory as the specified LAS or LAZ file. The LAX file contains spatial indexing information for the entire point cloud, encapsulated in a compact data format that enhances the efficiency of processing large datasets (Isenburg, 2023).

Ground classification: To classify the ground points, I applied the Simple Morphological Filter (SMRF) introduced by Pingel et al. (2013). The algorithm creates a minimum surface, then processes it to classify grid cells as either bare earth or objects. It then generates a DEM from the gridded points and categorizes the original LIDAR data based on its relationship to the interpolated DEM. The SMRF in LiDAR data processing is used to separate ground from non-ground points by determining whether raster cells contain bare earth (BE) or objects (OBJ). The filter works by progressively removing points that do not meet certain criteria based on their elevation and the elevation of surrounding points, considering the expected terrain features. It is designed to retain points that are part of the actual ground surface while filtering out points from vegetation and other above-ground structures. The non-ground points are discarded.

Inverse Distance Weighting (IDW) interpolation: By using IDW interpolation, I applied the IDW algorithm to the LiDAR point cloud data to interpolate values for the raster's pixels. This algorithm assigns values to the raster pixels based on the values of nearby points, with closer points having a greater influence on the pixel value than those further away. The influence is inversely related to the power of the distance, defined in this case as resolution times square root of 2. This process resulted in a set of 15 elevation data raster files, each corresponding to a flight round.

Offset calibration To minimize height discrepancies among the parallel lines and prevent abrupt elevation changes in areas of flight stripe overlap, I used one of the crossing stripes for height offset calibration. Since the west-east stripe intersects all other flight rounds, it served as the benchmark. I identified the shared overlap between each flight round (ordinary rounds) and the reference west-east round (master round). I then determined the height difference between the master- and each ordinary round, using the median values from their overlapping regions to adjust each raster accordingly. As a result, every pixel in an ordinary raster was adjusted up or down based on its median difference from the master flight loop (Table 2.3).

Table 2.3: Flight stripe elevations and offset data

id	flight stripe	max height (m)	min height (m)	median offset
1	ALS_L1B_20230402T163403_165031	175.11	-5.30132	0.01072
2	ALS_L1B_20230402T165028_170344	174.72	-5.07940	0.00993
3	ALS_L1B_20230402T170341_172013	184.60	-5.24631	-0.00456
4	ALS_L1B_20230402T172009_173551	185.24	-5.24671	-0.01097
5	ALS_L1B_20230402T173547_175135	184.21	-5.19181	-0.05138
6	ALS_L1B_20230402T175131_181008	191.49	-5.18000	-0.05234
7	ALS_L1B_20230402T181004_182441	182.55	-5.16177	-0.02995
8	ALS_L1B_20230402T182437_184004	188.23	-5.23753	-0.03185
9	ALS_L1B_20230402T184000_185547	188.03	-5.24401	-0.01629
10	ALS_L1B_20230402T185544_191120	188.28	-5.24991	-0.01787
11	ALS_L1B_20230402T191116_192642	188.17	-5.21000	-0.03765
12	ALS_L1B_20230402T192638_194109	188.15	-5.13993	-0.03207
13	ALS_L1B_20230402T194106_195556	188.17	-5.20183	-0.01163
14	ALS_L1B_20230402T201158_202822	164.00	-5.42596	0.00000
15	ALS_L1B_20230402T202818_203550	126.51	-5.43728	-0.00648

Merge stripes to DSM: To merge the independent offset calibrated flight rounds, I used GDAL in QGIS, aplying cubic convolution interpolation as the resampling method. The resulting product was a 1 m pixel GeoTIFF raster file winter snow-covered DSM.

2.1.2 DTM: snow free terrain

The DTM raster (DTM full) is a product of the summer campaign, which collected point-cloud data from the snow-free terrain of the Trail Valley Creek area. This data was acquired using a Riegl LMS-Q680i laser scanning sensor (RIEGL, 2012), onboard the POLAR-6 research aircraft on July 10, 2023. The raw data were converted into 3-dimensional points, with full-waveform properties for each laser return, by Veit Helm

(AWI). The data was further processed by Inge Grünberg (AWI) into GeoTIFF files with a 1 m cell size (Figure 2.3). This processing included identification and removal of vegetation based on full-waveform point characteristics. Additionally, a smoothed version of the DTM was created using a 7 m by 7 m kernel.

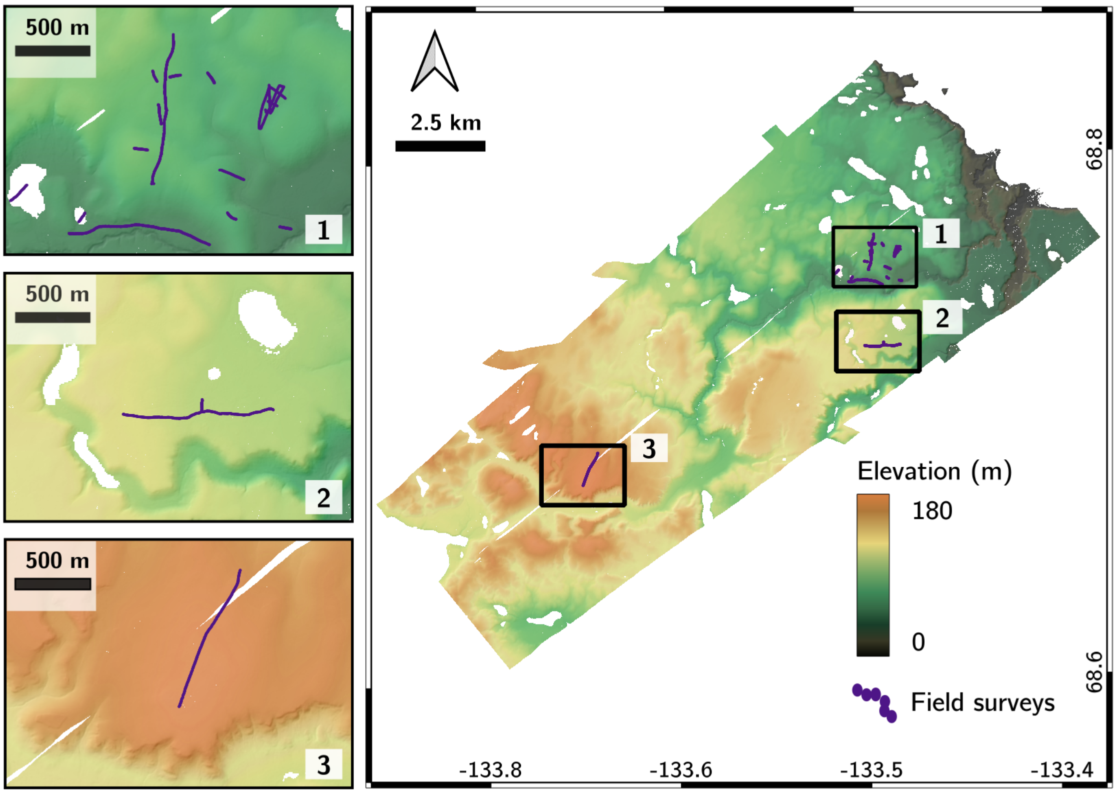

Figure 2.3: Snow-free DTM: LiDAR snow-free DTM from July 10, 2023 (Unpublished work, AWI, 2024a). As reference, the field snow depth survey locations from March 2023 (Rutter, 2023; Walker, 2023) are shown in purple, and detailed in the insets 1, 2, and 3. Regions with no data are represented in white.

2.1.3 Snow depth calculation

Calculating the difference between a snow-surface DSM and a snow-free bare ground elevation model, such as a DTM, is a widely used method for measuring snow depth (Dai et al., 2024; Deems et al., 2013; Walker et al., 2020). To create the LiDAR snow depth raster map used in this work, I used the snow-covered DSM from the LiDAR winter survey and from it I subtracted the elevation values of the snow-free DTM full from the summer survey 2023, as following:

$$\text{snow depth} = \text{DSM elevation}_{\text{snow covered}} - \text{DTM elevation}_{\text{snow free}}$$

2.1.4 Validation of the snow depth map

Validation based on the ITH control points

To set the control points along the ITH, I delineated the midpoint of the road as a line polygon layer on QGIS (QGIS Development Team, 2023), using the ESRI Satellite as basemap (Esri et al., 2023). I then segmented this line into points at 1 m intervals, resulting in a total of 9576 positions.

Next, I loaded the point vector file into R and extracted the LiDAR snow depth values at those coordinates. Before analysing the distribution of the snow depth values across those points, I identified and excluded 7 outliers by removing values that were more than three standard deviations away from the mean, reducing the dataset to 9569 points.

Validation based on field surveys

The field data consisted of 4615 snow depth points, measured between March 26 and 31, 2023, by Walker (2023) and Rutter (2023). These measurements were taken along multiple transects within our area of interest, located in the northeast region near the Trail Valley Creek research station, and in the southwest region. The summary of transects is provided in Table 2.4, and the survey locations are included in all plotted maps for reference.

Table 2.4: Field survey summary: Field snow depth surveys with their corresponding date, their location, the amount of samples at each transect, and the researcher responsible for the measurements, Rutter (2023), and Walker (2023).

Date	Location	Sample count	Researcher
26.03.2023	Main Met	925	Rutter
28.03.2023	Forest	581	Rutter
28.03.2023	Valley	1037	Rutter
29.03.2023	Upper Plateau	586	Rutter
26.03.2023	IWP	402	Walker
28.03.2023	TMM	185	Walker
28.03.2023	LYS	53	Walker
28.03.2023	TFS	86	Walker
28.03.2023	LBL	58	Walker
28.03.2023	BBL	122	Walker
30.03.2023	SLB	103	Walker
30.03.2023	SLT	100	Walker
30.03.2023	STS	97	Walker
31.03.2023	STB	99	Walker
31.03.2023	SMT	88	Walker
31.03.2023	SMC	93	Walker

The field sampling method used involved inserting a magnetostrictive metal probing rod (Magnaprobe) through the snowpack. Once inserted, the Magnaprobe measures the distance between its tip at the bottom, where it interfaces with the ground surface, and a sliding disk that marks the snow's upper limit, along with the survey position (Sturm and Holmgren, 2018).

Aiming to gap the scale difference between point data and LiDAR pixel estimates, I used a buffering method to average the field snow depths in R. First, I retrieved the position of each snow depth measurement that matched a valid LiDAR snow depth raster pixel. Then, I set a 5 m buffer around each LiDAR pixel and averaged the field snow depth points within this area. This buffer average was then assumed to be the field snow depth representative for the LiDAR pixel. The choice for buffering was an attempt to counteract accuracy limits of the field GPS and because of the gap in scale between point measurements and pixel averages. After filtering out field survey points that were not within the LiDAR snow depth map, and averaging the measurements within the buffer area, the final dataset comprised 3964 field snow depth records matched with LiDAR pixels.

2.2 Topography datasets

2.2.1 Mapping landforms with the geomorphons approach

The geomorphons method is a technique used in geomorphology and remote sensing to classify and analyze landforms based on their shape and structure. It relies on pattern recognition algorithms to identify and categorize typical landform elements, called geomorphons (geometric morphologies). The geomorphons method analyses the spatial arrangement of raster cells in a DTM, based on their line-of-sight neighbors. In this context, the elevation value of a central pixel is compared with the values of eight surrounding neighbors and subsequently categorized according to its pattern (Jasiewicz and Stepinski, 2013). Since the neighborhood is not fixed in size, the designated 'visible-neighbor' pixel may not be an immediate adjacent cell.

To define this line-of-sight zone, the user specifies two parameters: the flatness threshold (t), which sets the maximum slope (in degrees) below which the terrain is classified as flat, and the outer search radius/search distance (L), which defines the radius of the neighborhood. Figure 2.4 presents different geomorphon maps created with the smoothed DTM as input, using different parameter combinations. In this demonstration, I tested flatness thresholds of 1, 2, and 5 degrees and the outer search radii/search distance of 90 m and 250 m.

The classification of the DTM produces a geomorphon map, categorizing the terrain into ten distinct landforms: flat, summit, ridge, shoulder, spur, slope, hollow, footslope, valley and depression. I implemented this method using the r.geomorphon extension (GRASS Development Team, 2023) in QGIS 3.32 Lima (QGIS Development Team, 2023), with parameters detailed in Table 2.5. After generating the initial 10-class geomorphons landform map, I simplified the map by combining similar classes.

- Flat class remains unchanged.
- Summit and ridge classes were combined as ridge.
- Shoulder and spur classes were merged as shoulder.

- Slope class remains unchanged.
- Hollow and footslope classes were consolidated as footslope.
- Valley and depression classes were merged as valley.

This simplification process resulted in a 6-class landform map, featuring the classes: flat, ridge, shoulder, slope, footslope, and valley (Fig 3.7).

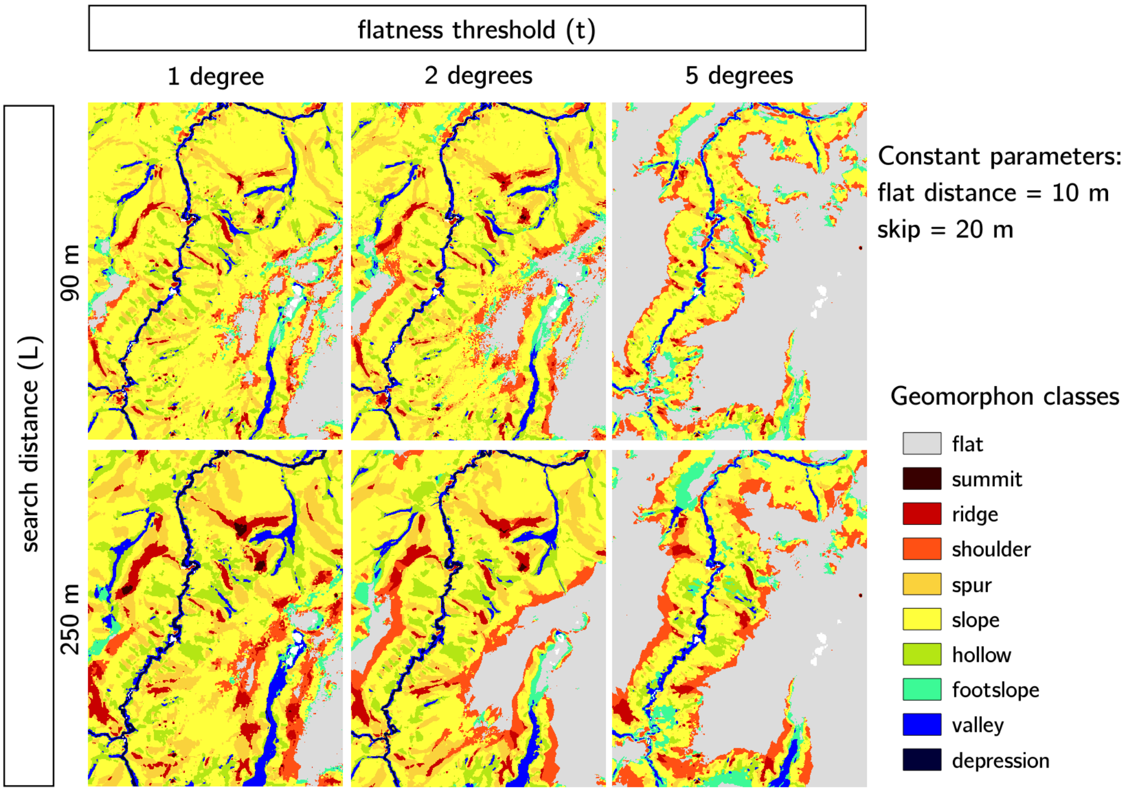

Figure 2.4: Geomorphon classification examples: Demonstration of geomorphon map outputs with varying input parameters for the flatness threshold (t), and outer search radius/search distance (L) in r.geomorphons. In all outputs, the flatness distance parameter was fixed at $10\,\mathrm{m}$, and the inner search radius/skip at $20\,\mathrm{m}$. For this work, I chose the flatness threshold (t) $= 2°$ and outer search radius/search distance (L) $= 250\,\mathrm{m}$.

Table 2.5: r.geomorphons parameters used for the classification of landforms

Parameter	**Value**
Digital elevation model input	Summer smoothed DTM 1 m resolution
Outer search radius/search distance (L)	250 m
Inner search radius/skip	20 m
Flatness threshold (t)	2°
Flatness distance	10 m

2.2.2 Mapping slope and aspect

I used the R packages ‘raster’ and ‘terra’ to extract the slope and aspect values in each pixel from the smoothed DTM, creating a 1-m per pixel slope and aspect rasters. I then categorized the slope raster into four steepness ranges: flat ($< 1°$), slight ($1° \leq \theta < 3°$), moderate ($3° \leq \theta < 5°$), and steep ($> 5°$). I categorized the aspect values into eight classes, representing the cardinal and intercardinal directions: north, northeast, east, southeast, south, southwest, west, and northwest. I then combined these variables as a matrix of 32 unique classes (4 slope ranges x 8 aspect classes), where each cell in this matrix represents an unique combination of slope steepness and aspect category.

2.3 Vegetation datasets

2.3.1 Classifying vegetation height

The most recent vegetation height map from Trail Valley Creek (Unpublished work, AWI, 2024b) is based on the full-waveform summer 2023 LiDAR survey. The vegetation height values were derived by subtracting the DTM raster from all LiDAR returns and taking the maximum height for each pixel. LiDAR returns more than 20 m above the DTM were removed as outliers. I used the vegetation height map and categorized it into four ranges: under 0.1 m, 0.1 - 0.5 m, 0.5 - 1.5 m, and above 1.5 m (Fig 2.5).

2.3.2 Vegetation class map

The latest AWI vegetation class map of Trail Valley Creek (Unpublished work, Grünberg, 2024) distinguishes 13 classes among vegetation types and land cover features (Figure 2.6), and is based on the summer LiDAR survey from 2018 (Lange et al., 2021).

For this analysis, I excluded large water bodies by removing the lake class from the vegetation map. LiDAR pulses interact differently with water surfaces than with solid terrain, leading to inaccuracies and data gaps over large water bodies in all LiDAR-derived datasets. This adjustment resulted in a vegetation class map with 12 classes, as shown in Figure 2.7.

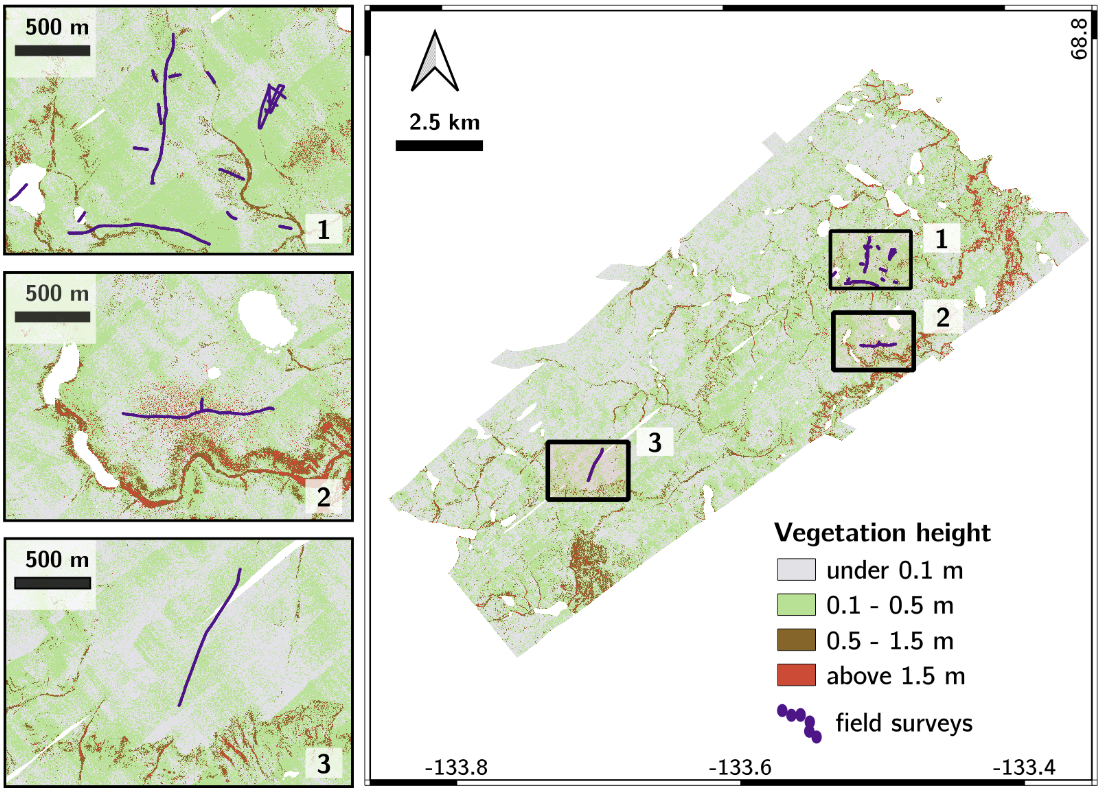

Figure 2.5: Vegetation height classes: LiDAR vegetation height map from the summer campaign in July 2023, classified into four height ranges (Unpublished work, AWI, 2024b). As reference, the field snow depth survey locations from March 2023 (Rutter, 2023; Walker, 2023) are shown in purple, and detailed in the insets 1, 2, and 3. Regions with no data are represented in white.

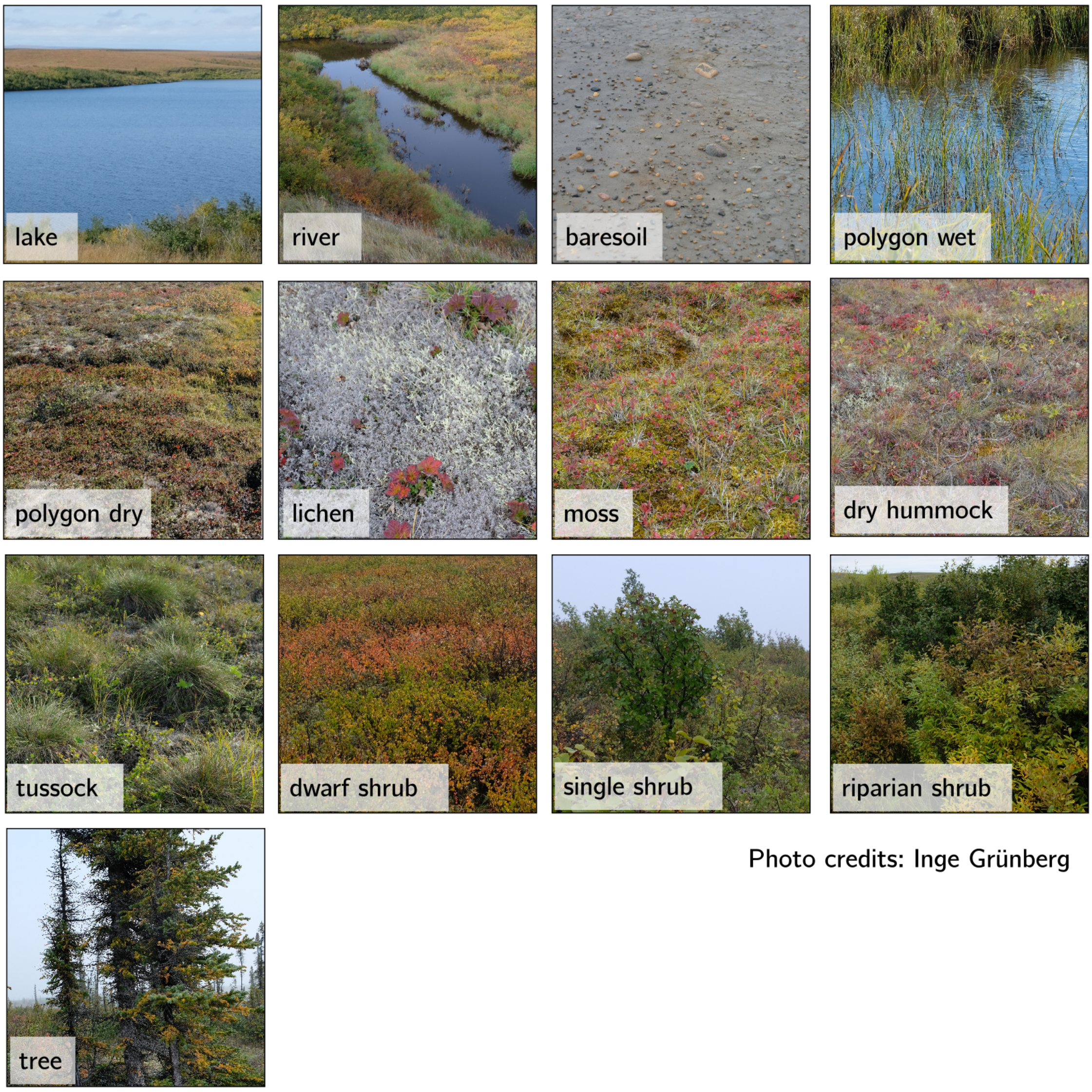

Figure 2.6: Vegetation cover examples: Vegetation cover in Trail Valley Creek, represented across 13 classes based on unpublished work by Inge Grünberg (Grünberg, 2024). Each class is illustrated with photographs from the study area.

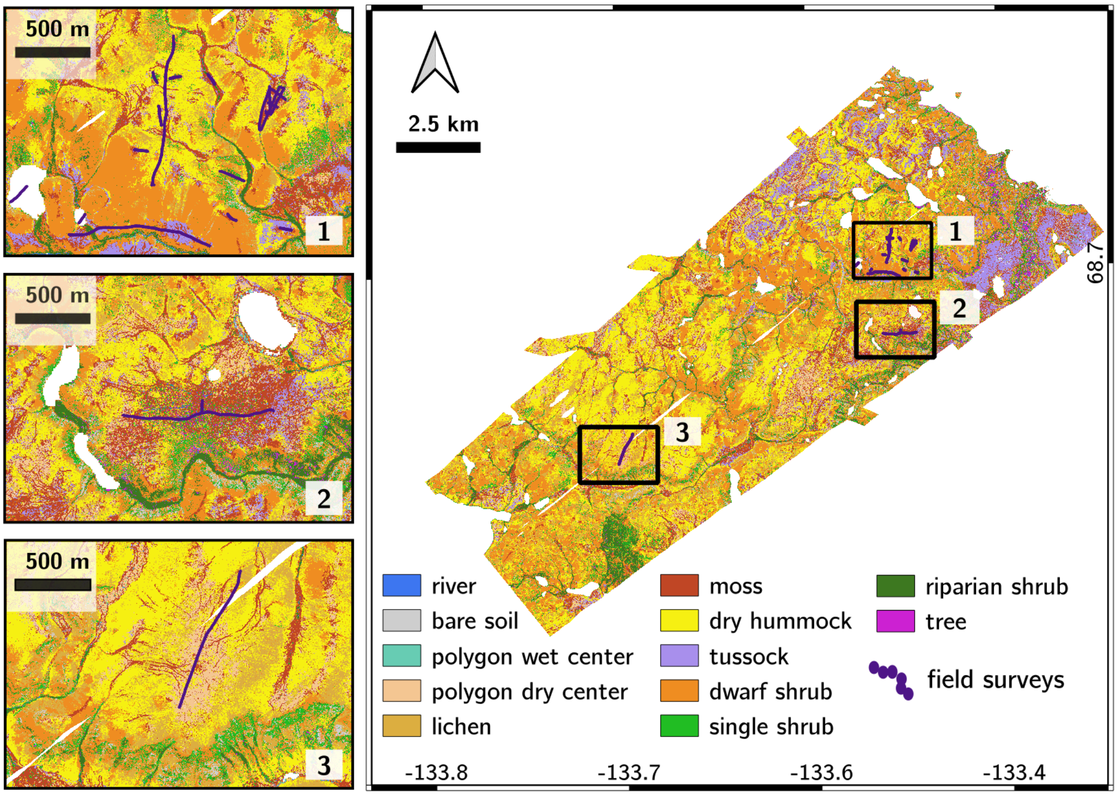

Figure 2.7: Vegetation class map: The vegetation class map used in this work, adapted from Grünberg (2024). As reference, the field snow depth survey locations from March 2023 (Rutter, 2023; Walker, 2023) are shown in purple, and detailed in the insets 1, 2, and 3. Regions with no data are represented in white.

2.4 Data analysis

To maintain consistency in the datasets and analysis, I ensured that all rasters covered the same spatial extent and that each pixel contained valid data across all datasets. This approach guaranteed that every pixel at a given position has valid values for snow depth, landform, slope, aspect, vegetation, and vegetation height.

Once the maps shared the same extent throughout, I used the DSM raster as a reference and resampled the remaining ones, using the nearest neighbor method to match the reference. I then cropped the rasters to their common intersection extent, stacked them, and created an invalid mask to identify NA pixels throughout the stack. Based on this mask, I excluded the invalid pixels from each of the stacked rasters. This process ensured that the final dataset excluded large water bodies (as they had been previously excluded from the vegetation class map) and maintained consistency across all rasters, with each pixel having valid data for all parameters. All rasters were projected using UTM Zone 8N, WGS84 datum, with units in meters (EPSG:32608).

2.4.1 Snow depth map: metrics, distribution, and validation

To understand the distribution of the snow depth raster, I converted the GeoTIFF file to a dataframe and calculated distribution statistics, including maximum, minimum, mean, median, range, standard deviation, variance, and interquartile range. I then plotted a histogram to visualize the overall distribution pattern. For mapping in QGIS (QGIS Development Team, 2023), I categorized the snow depths to emphasize the central distribution, while still using the full snow depth map throughout the analysis.

To validate the LiDAR-derived snow depth map, I used two reference methods: reference control coordinates over the ITH, and field survey snow depth measurements. Since the ITH is constantly snow-plowed during winter (Hammar et al., 2023), I assumed a snow depth at the road midpoint to be zero for this analysis. Using R, I extracted snow depth values from the LiDAR snow depth map at each of the 9569 ITH-point reference coordinates. I then calculated the distribution statistics for this dataset, including maximum, minimum, mean, median, range, standard deviation, variance, and interquartile range, and visualized these values with a histogram. Similarly, I used the reference coordinates from the field surveys to extract the LiDAR snow depths at those points. I calculated distribution statistics, including maximum, minimum, mean, median, range, standard deviation, variance, and interquartile range, as well as the correlation coefficient and the median of differences between field survey and LiDAR at each of the 3964 points. To visualize the distributions of both methods, I used paired histograms to display the overall spread and central tendency. To assess agreement between the field and LiDAR snow depths, I used a Bland-Altman plot-a scatterplot that shows the differences between paired measurements on the y-axis and the averages of the two measurements on the x-axis-to identify systematic biases, outliers, and discrepancies between the two methods.

2.4.2 Linking snow depths, topography and vegetation

To investigate the relationships among snow depth, topography, and vegetation, I converted the GeoTIFF files for landform, slope, aspect, vegetation height, and vegetation class into dataframes, and merged them to the LiDAR snow depths. Once each variable was matched to the LiDAR values, I calculated the snow depth distribution within each of their associated classes, including metrics such as maximum, minimum, mean, median, range, standard deviation, variance, interquartile range, skewness, and kurtosis (see Appendix for related tables). I used violin plots-which display the distribution of data by combining a box plot with a kernel density plot-to illustrate the snow depth distribution for each variable. Beside the the data spread across classes, the plots also display their respective medians and quantiles.

In a second step, I compare LiDAR snow depths to the field surveys once again. This time, I classified the field surveys according to their landform, slope, aspect, vegetation height, and vegetation class categories, and calculated the paired distribution statistics (maximum, minimum, mean, median, range, standard deviation, variance, interquartile range, correlation coefficient and the median of differences) according to their respective classes. The classified distribution of the paired methods was displayed as boxplots, and excluded all classes below a minimum threshold of 10 measurements. The related tables can be found in the Appendix section.

Results

3.1 Snow depth map

The LiDAR snow depth map for Trail Valley Creek (Figure 3.4), was based on the snow-covered DSM of April 2, 2023 (shown in Figure 3.3), and covered an area of 127 704 691 m^2. The map had a snow depth mean of 0.35 m and a median of 0.30 m, suggesting a skew toward higher values. While the total range spanned from -7.61 m to 8.15 m, the central 99% of the data, which excludes the most extreme 0.5% on both ends, fell within the range of 0.00 m and 1.60 m (Table 3.1). A standard deviation of 0.24 m reflected moderate variability around the mean, while the interquartile range (IQR) of 0.20 m indicated that the central 50% of values were closely clustered around the median.

Table 3.1: LiDAR snow depth distribution

mean (m)	median (m)	min (m)	max (m)	SD (m)	var (m^2)	range (m)	IQR (m)	skewness	kurtosis
0.3503	0.2976	-7.6077	8.1530	0.2434	0.0593	15.7608	0.2041	3.3662	24.8194

*SD = Standard Deviation; IQR = Interquartile Range.

The histogram (Figure 3.1) showed a pronounced peak near the median value, with most snow depths concentrated below 0.5 m and diminishing gradually toward higher values. A skewness of 3.37 confirmed a rightward skew, while the kurtosis of 24.82 highlighted a strong peak with heavy tails, indicating that most values were concentrated near the center, with occasional extreme depths. The histogram also showed quartile markers: Q1 at 0.21 m and Q3 at 0.42 m, emphasizing the central clustering of the snow depth values. The spatial patterns of snow depth will be presented and discussed in greater detail in the following sections.

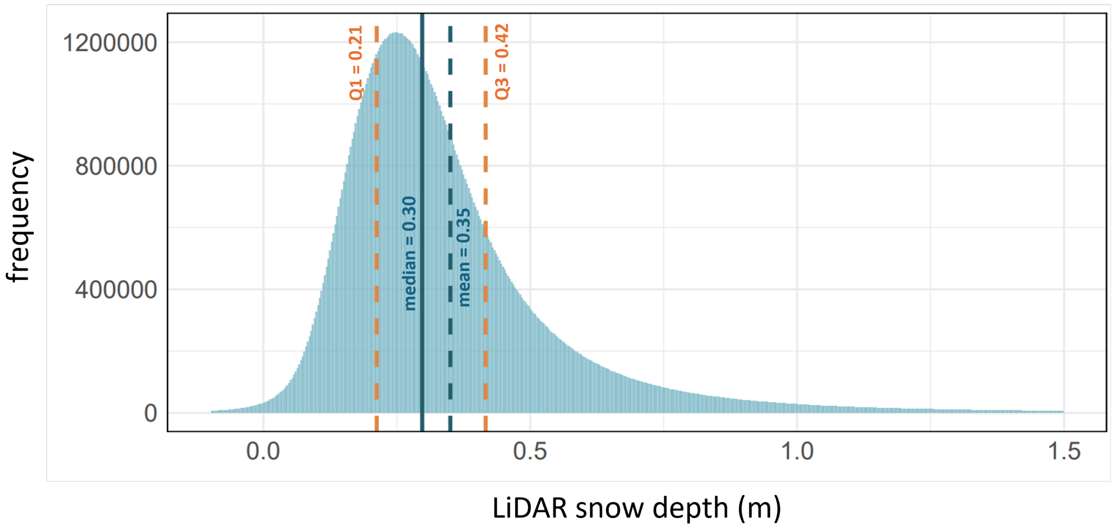

Figure 3.1: LiDAR snow depth distribution: Histogram of LiDAR snow depth distribution for Trail Valley Creek on April 2, 2023. Orange dashed lines represent the first and third quartiles (Q1 $= 0.21\,\mathrm{m}$, Q3 $= 0.42\,\mathrm{m}$), while the mean is marked with a blue dashed line ($0.35\,\mathrm{m}$), and the median with a solid blue line ($0.30\,\mathrm{m}$).

3.1.1 Comparison to ITH control points

The distribution of LiDAR snow depth values across the midpoints of ITH section reveals generally low variability. As summarized in Table 3.2, snow depths ranged from $-0.143\,\mathrm{m}$ to $0.323\,\mathrm{m}$, with a mean of $0.018\,\mathrm{m}$ and a median of $0.017\,\mathrm{m}$. The standard deviation ($0.047\,\mathrm{m}$) further indicates low variability across the points. The interquartile range showed that 50% of snow depth values are clustered within a $0.071\,\mathrm{m}$ band. The histogram of snow depths (Figure 3.2) demonstrates a nearly symmetric distribution with a subtle skew towards positive values.

Table 3.2: Snow depth distribution along the Inuvik-Tuktoyaktuk Highway

count	mean (m)	median (m)	min (m)	max (m)	SD (m)	variance (m^2)	range (m)	IQR (m)
9569	0.0179	0.0166	-0.1426	0.3232	0.0469	0.0022	0.4658	0.0707

*SD = Standard Deviation; IQR = Interquartile Range.

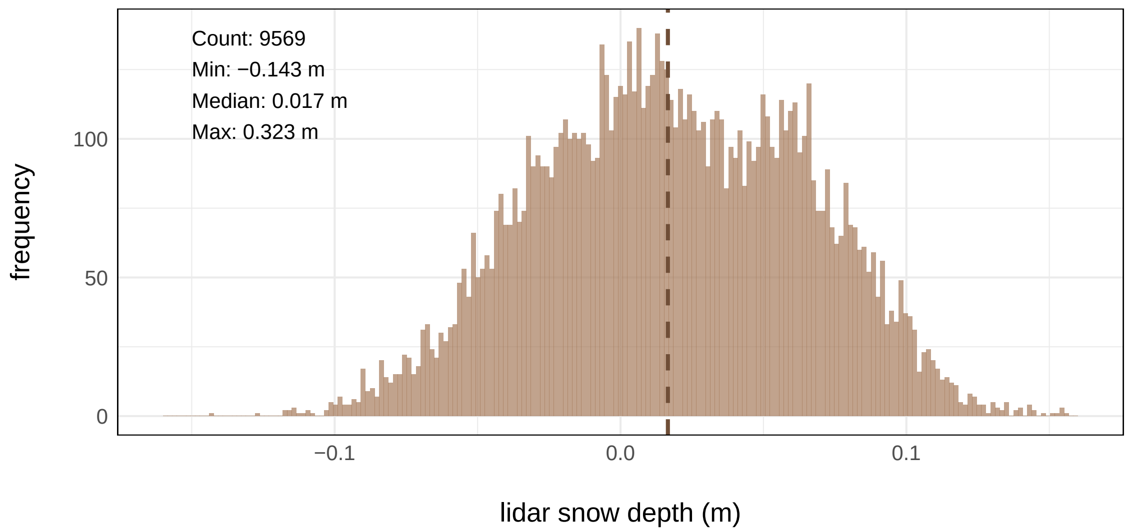

Figure 3.2: ITH snow distribution histogram: Histogram of LiDAR snow depth values along the ITH. The 9,569 points were referenced at midpoint of the road, spaced at 1 m, along the road section that intersects the study area. The brown dashed line indicates the median snow depth value.

3.1.2 Comparison to field surveys

General distribution

If the snow depths along the ITH control points showed a median bias lower than 0.02 m, the pattern over the natural landscape of Trail Valley Creek revealed different trends.

Table 3.3: LiDAR and field survey snow depth values general distribution

method	count	mean (m)	median (m)	min (m)	max (m)	SD (m)	variance (m^2)	range (m)	IQR (m)	r	med dif (m)
field	3964	0.521	0.471	0.183	1.38	0.185	0.0341	1.19	0.215	0.788	0.179
lidar	3964	0.346	0.314	-0.0119	1.62	0.188	0.0352	1.63	0.213	0.788	0.179

*SD = Standard Deviation; IQR = Interquartile Range.

Among the 3964 paired data points, field measurements exceeded LiDAR values in 93% of cases (3684 points), highlighting the general tendency for field snow depths to be higher. As seen in Table 3.3, the field measurements showed a mean snow depth of 0.521 m, a median of 0.471 m, with a standard deviation of 0.185 m. In contrast, LiDAR measurements had a lower mean of 0.346 m and a median of 0.314 m, with a slightly higher standard deviation of 0.188 m. The interquartile range for field measurements was 0.215 m, while for LiDAR, it was 0.213 m, both of which reflect similar ranges in the central 50% of their respective datasets. Additionally, the minimum values for LiDAR snow depth were negative, with a value of −0.012 m, while the field measurements had a minimum of 0.183 m. The maximum depth for

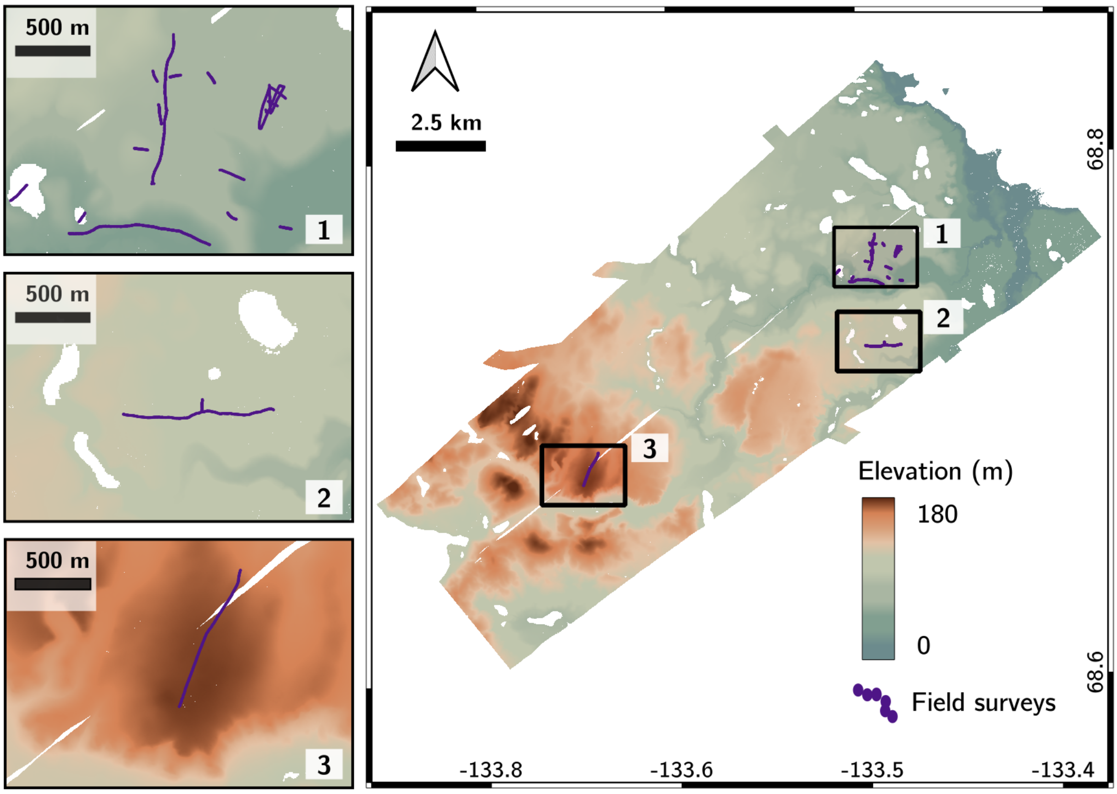

Figure 3.3: Snow-covered DSM: LiDAR snow-covered DSM from April 2, 2023. As reference, the field snow depth survey locations from March 2023 (Rutter, 2023; Walker, 2023) are shown in purple, and detailed in the insets 1, 2, and 3. Regions with no data are represented in white.

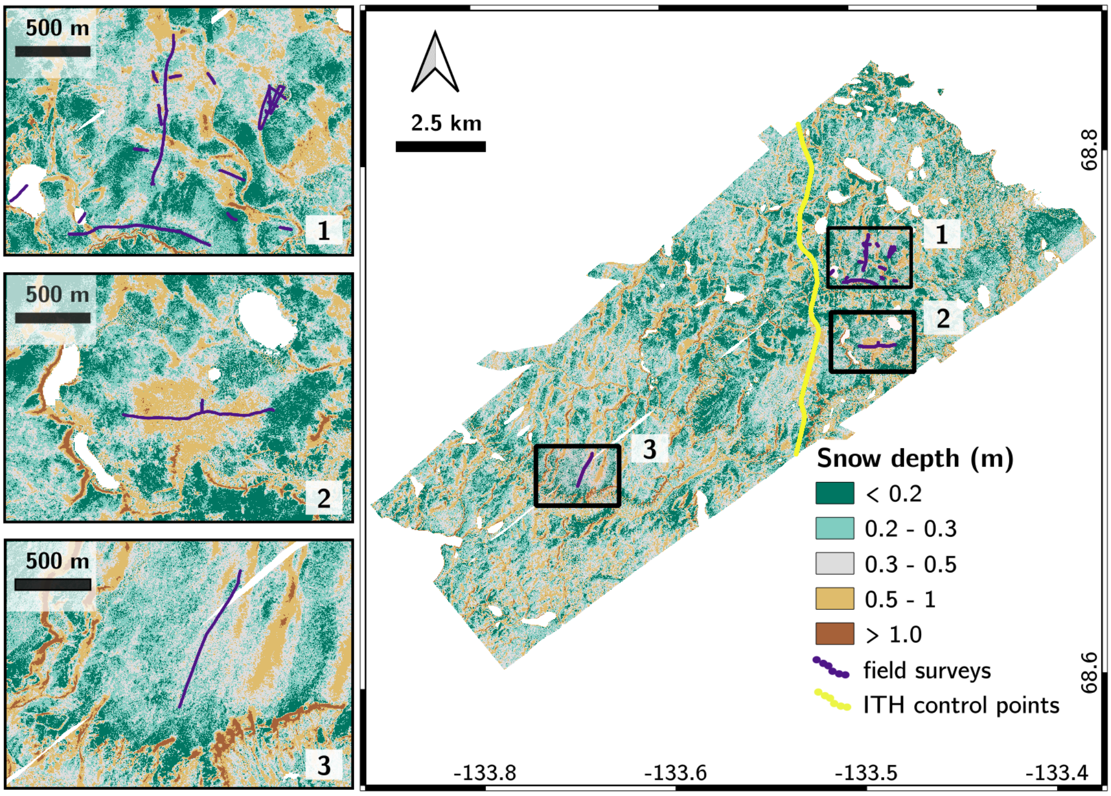

Figure 3.4: Snow depth map: Trail Valley Creek snow depth map derived from differencing the snow-covered DSM from April 2, 2023, and the snow-free DTM from July 10, 2023. Field snow depth survey locations from March 2023 (Rutter, 2023; Walker, 2023) are shown in purple, and detailed in insets 1, 2, and 3. Control points along the ITH are displayed in yellow, with regions of no data represented in white.

LiDAR was slightly higher (1.62 m) compared to the field measurements (1.38 m), indicating a broader spread of values in LiDAR measurements. The table also highlights a median of differences (med dif) of 0.179 m between field and LiDAR measurements, reinforcing the central tendency for the field measurements to be higher than LiDAR. Furthermore, the correlation coefficient (r) of 0.788 suggested a strong positive relationship between the two methods, meaning that despite the differences in absolute values, LiDAR and field measurements generally follow similar snow depth patterns across the study area.

The Bland-Altman plot, which here presents the differences between field and LiDAR snow depths, plotted against their averages (Figure 3.9), further highlights the differences between both methods. It shows the mean difference between field and LiDAR measurements as 0.175 m, with the upper limit of agreement (LoA) at 0.412 m and the lower LoA at -0.063 m. It demonstrated that 95% of the data points fell within these bounds, although there was a clear tendency for field measurements to be higher than LiDAR, as shown by the concentration of points above the zero difference line. The similarity between the mean difference (0.175 m) and the median of differences (0.179 m) indicates that the distribution of differences between field and LiDAR measurements is relatively symmetrical, with few extreme outliers. The histogram (Figure 3.6) reinforces these findings, where the field measurements (in blue) were shifted toward higher snow depths, with a median value of 0.47 m, compared to the LiDAR measurements (in orange), which had a median of 0.31 m. Both distributions showed similar overall shapes, but the LiDAR data was skewed toward lower values, resulting in a larger proportion of negative snow depths compared to the field data.

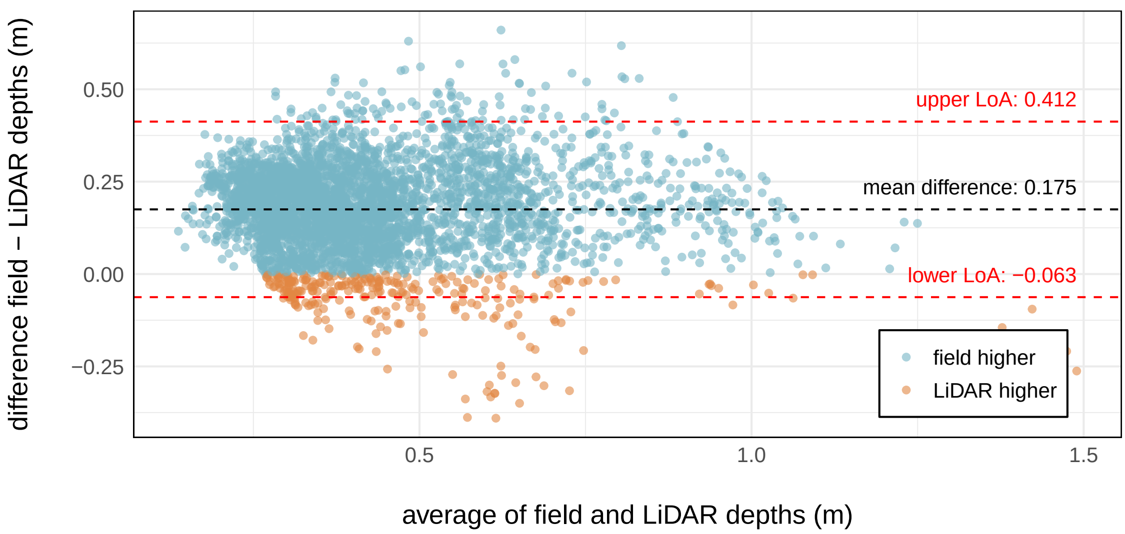

Figure 3.5: Bland-Altman diagram: The Bland-Altman diagram illustrates the differences between field and LiDAR snow depths. Blue points indicate where field measurements are higher than LiDAR, while orange points show where LiDAR depths are greater. The red lines represent the upper and lower limits of agreement (LoAs), with 95% of the differences falling between -0.063 and 0.412 m. The black dashed line represents the mean difference.

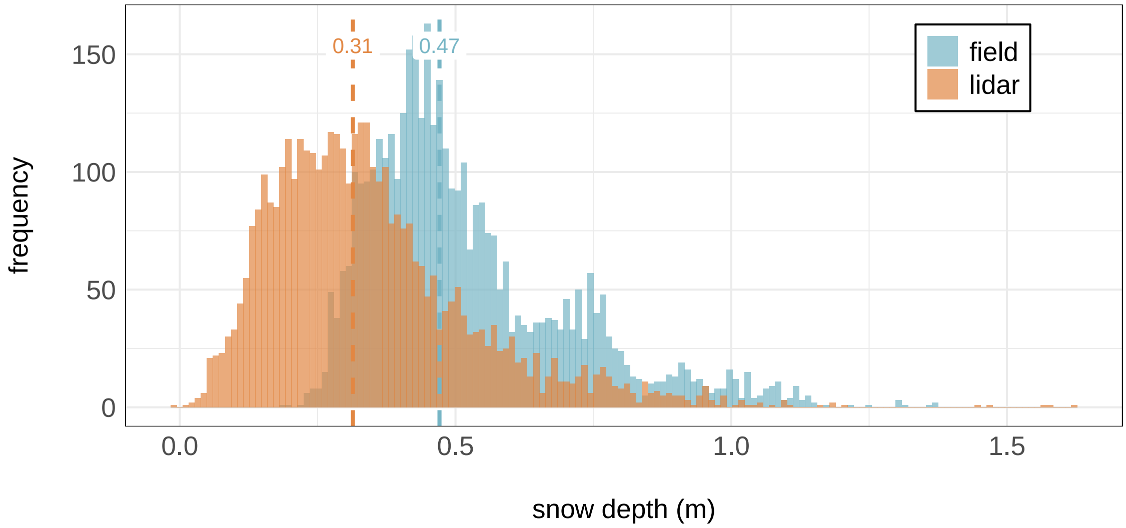

Figure 3.6: Field and LiDAR snow depth distribution: Snow depth distribution of the pixel-averaged field measurements (in blue) and LiDAR (in orange). The dashed lines represent the medians (Lidar = $0.31\,\mathrm{m}$, field = $0.47\,\mathrm{m}$)

3.2 Snow depth and topography

3.2.1 Landforms

The area was divided into 6 landform classes, in a simplified version of the geomorphons approach landscape classification from Jasiewicz and Stepinski (2013). Most of the area is represented by slopes, covering 39.8 km^2, followed by flat areas with 33.5 km^2 and shoulder regions with 24.8 km^2. Footslope and valley areas cover 14.9 km^2 and 6.9 km^2, respectively, while ridges account for the smallest area at 7.8 km^2. The total mapped area amounts to 127.7 km^2 (Figure 3.7).

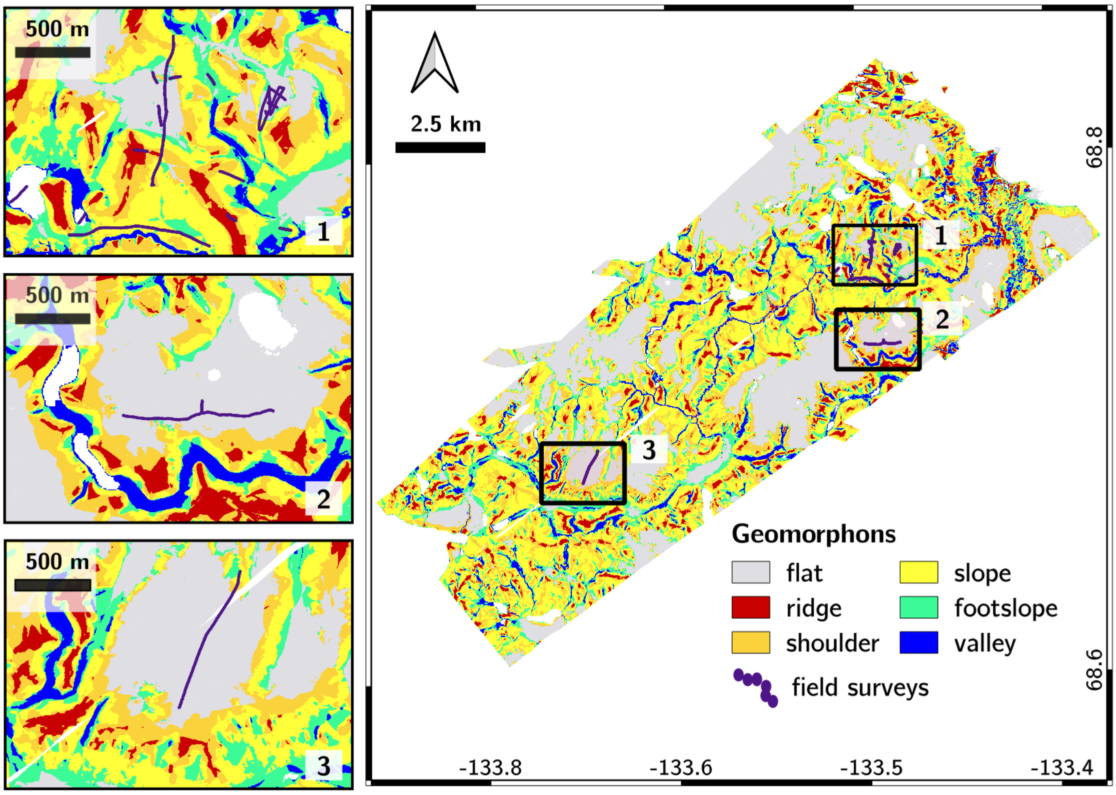

Figure 3.7: Landform map: Created with the geomorphons classification approach by Jasiewicz and Stepinski (2013), using the DTM smoothed. As reference, the field snow depth survey locations from March 2023 (Rutter, 2023; Walker, 2023) are shown in purple, and detailed in the insets 1, 2, and 3. Regions with no data are represented in white.

The snow depth distribution across landforms, demonstrated distinct patterns in both central tendencies and variability. On ridges, the mean and median snow depths were the lowest, at 0.22 m and 0.20 m respectively, while in valleys, they were the highest, at 0.53 m and 0.44 m. Footslopes and valleys consistently showed higher snow depths compared to ridges and shoulder areas, as demonstrated in the violin plot (Figure 3.8). In terms of variability, footslopes and valleys exhibited the highest standard deviations (0.33 m and 0.38 m, respectively), indicating greater spread in snow depth values, while flat and ridge areas had lower variability with standard deviations of 0.13 m in both cases. The interquartile range followed a similar pattern, with the widest ranges observed in valleys (0.36 m) and footslopes (0.28 m), while flat areas and ridges showed the narrowest ranges (0.14 m and 0.13 m, respectively). These patterns are captured visually in the violin plot, where the elongated shapes correspond to greater variability in snow depths, particularly in the valley and footslope classes. Regarding skewness, the footslope areas exhibited the highest skewness value of 3.07, followed closely by shoulder and slope classes, both with skewness values of 2.99, indicating a strong positive skew. In contrast, flat areas had a skewness of 1.80, and ridge areas had the lowest skewness at 1.57, both of which reflect a more moderate positive skew, indicating that snow depth values in these classes are more symmetrically distributed compared to the others. Kurtosis values were highest in ridge and shoulder areas, reflecting sharper, more peaked distributions with a higher likelihood of extreme outliers. Conversely, flat and valley areas exhibited lower kurtosis, indicating more evenly spread snow depth values around the mean.

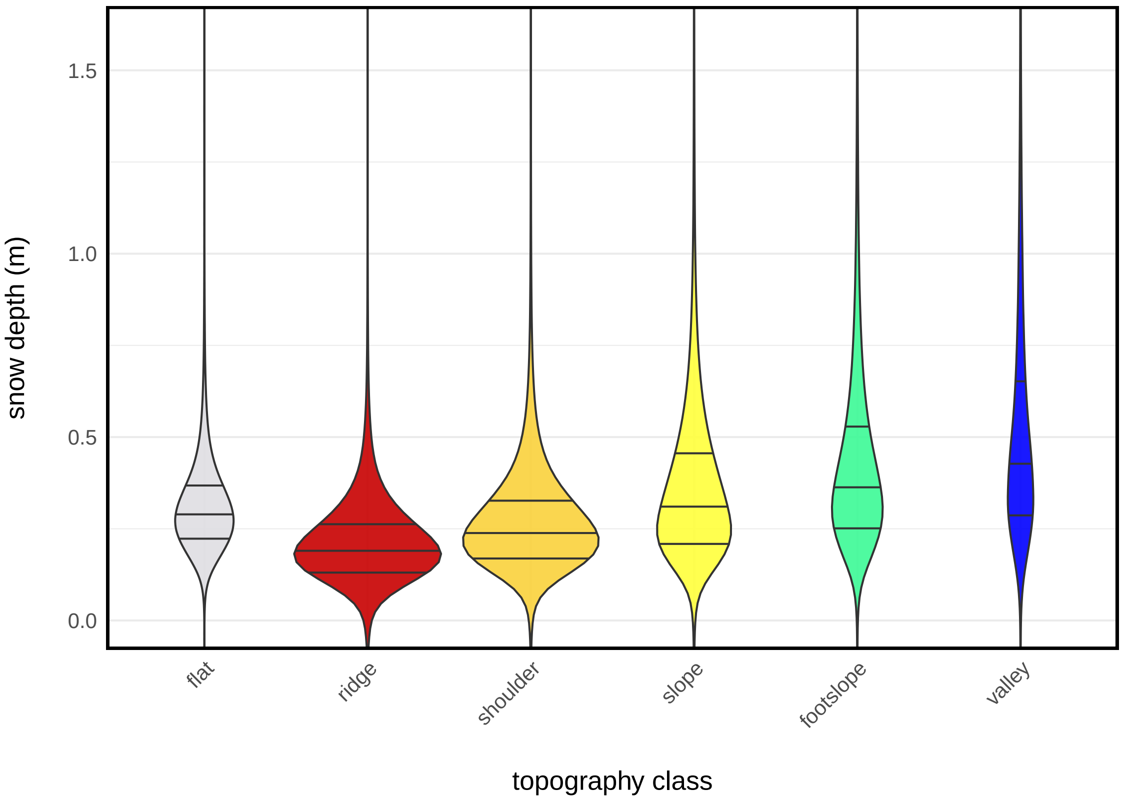

Figure 3.8: Snow depth distribution across landform classes: This violin plot displays the distribution of the central 99% of the LiDAR snow depth data for each landform class, with snow depth (m) on the y-axis. Each violin shows the density curve of the snow depth values, with the internal lines marking the corresponding median and quartiles.

Landforms and field surveys

To assess whether geomorphology impact the bias in LiDAR snow depth estimations, I classified the field surveys based on their corresponding landform categories. Field measurements were not available for the valley landform class, leaving this landform exclusively represented by LiDAR measurements in the analysis.

The comparison between LiDAR and field snow depth measurements across landform classes revealed patterns of bias and variability, but maintained the general trend, with field surveys recording higher snow depths across all classes. The median of differences ranged from 0.14 m in flat areas to 0.24 m in ridge areas, reflecting a variable bias across the terrain types (Figure 3.9). Ridges also exhibited the weakest correlation (r = 0.61), indicating a lower agreement between field and LiDAR in these regions. In contrast, footslopes (r = 0.89) and shoulder areas (r = 0.83), displayed the highest agreement, suggesting a stronger alignment.

The variability of snow depths, as reflected by standard deviations, showed similar trends between field and LiDAR measurements across all landform classes. In the field data, standard deviations ranged from 0.05 m on ridges to 0.25 m in footslopes, while for LiDAR, the range was from 0.06 m on ridges to 0.26 m in footslopes. This consistent variability between field and LiDAR measurements suggests agreement in the overall spread of snow depth values across different landforms, despite the existing bias in their central tendencies. The interquartile ranges of LiDAR exceeded those of field surveys in ridges, slopes, and footslopes, indicating that LiDAR captures broader variability in these terrains, whereas field measurements showed a relatively narrower spread.

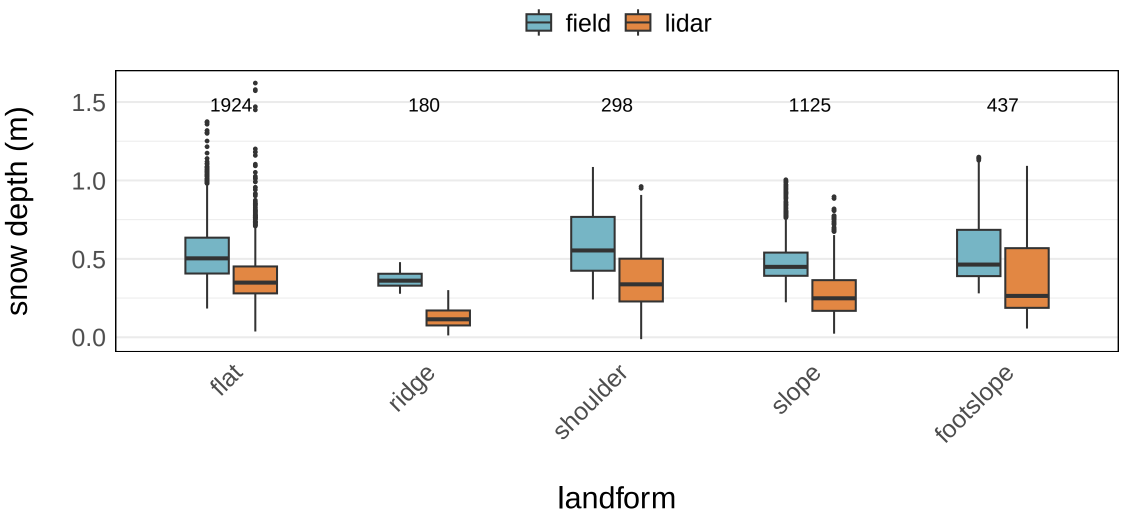

Figure 3.9: Pairwise LiDAR and field measurements across landform classes: Comparison of LiDAR (orange) and field (blue) snow depth measurements across landforms. Snow depth (m) is shown on the y-axis, with each pair of boxplots representing the depth distribution for each landform class. Sample sizes are indicated above each pair.

3.2.2 Slope and aspect

Following the investigation of how landforms relate to snow depth variability, I extended the analysis by comparing different slope classes and their associated aspects against the LiDAR-derived snow depth map. Slopes were categorized into four classes (flat, slight, moderate, and steep), and further divided into cardinal (N, E, S, W) and intercardinal (NE, SE, SW, NW) aspect classes to assess how these combined factors influence snow distribution.

When considering slope alone, snow depths increased with steepness. Median snow depth on steep slopes was nearly 0.08 m higher than on flat slopes, while the mean was approximately 0.15 m greater. Standard deviations and interquartile ranges also increased progressively, indicating a broader spread of snow depths as slopes became steeper.

The inclusion of aspect in the analysis revealed that both slope steepness and its associated aspect play a significant role in snow depth distribution. Steep, east-facing slopes had the highest median snow depth at 0.53 m, closely followed by southeast-facing slopes at 0.49 m. In contrast, flatter slopes exhibited lower median snow depths across all aspects, ranging between at 0.26 m and 0.29 m. West and northwest-facing slopes consistently recorded lower snow depths than east and southeast aspects within the same slope category, as demonstrated in Figures 3.11 and 3.12, highlighting the role of aspect on snow distribution.

Although snow depth variability increased with slope steepness overall, steep slopes facing east and southeast exhibited the greatest variability, with standard deviations reaching up to 0.45 m. This heightened variability was further evidenced by the wider interquartile ranges observed on these slopes, with the steep-east and steep-southeast classes recording interquartile ranges of 0.43 m and 0.39 m, respectively. In contrast, flatter slopes showed the least variability across all aspects, with standard deviation values consistently around 0.13 m and narrow interquartile ranges of 0.14 m, indicating more uniform snow depth distributions on flat terrain regardless of aspect.

Slope, aspect, and field surveys

Similar to the classification by landforms, the classification of field surveys according to slope and aspect revealed characteristic snow depth patterns. However, the sampling area was uneven, with over 80% of measurements taken in flat and slight slope areas and less than 4% in steep slopes (Figure 3.10). This limited coverage in steeper slope areas reduces the robustness of statistical analysis for these classes.

When considering steepness only, the field measurements consistently showed higher values than LiDAR across all 4 slope classes. Both means and medians increased with slope steepness, and the median of differences between field and LiDAR measurements followed a similar trend, ranging from 0.17 m in flat areas to 0.19 m in moderate slopes, and increasing to 0.29 m in steep slopes. Correlation coefficients indicated strong agreement in flat ($r = 0.78$), slight ($r = 0.80$), and moderate slopes ($r = 0.82$), but decreased sharply in steep slopes ($r = 0.62$), suggesting a larger discrepancy at higher gradients.

Aspect added further detail to this relationship: in flat and slight slopes, field and LiDAR measurements had similar standard deviations across all aspects, suggesting consistent variability. However, as slope increased, LiDAR snow depths

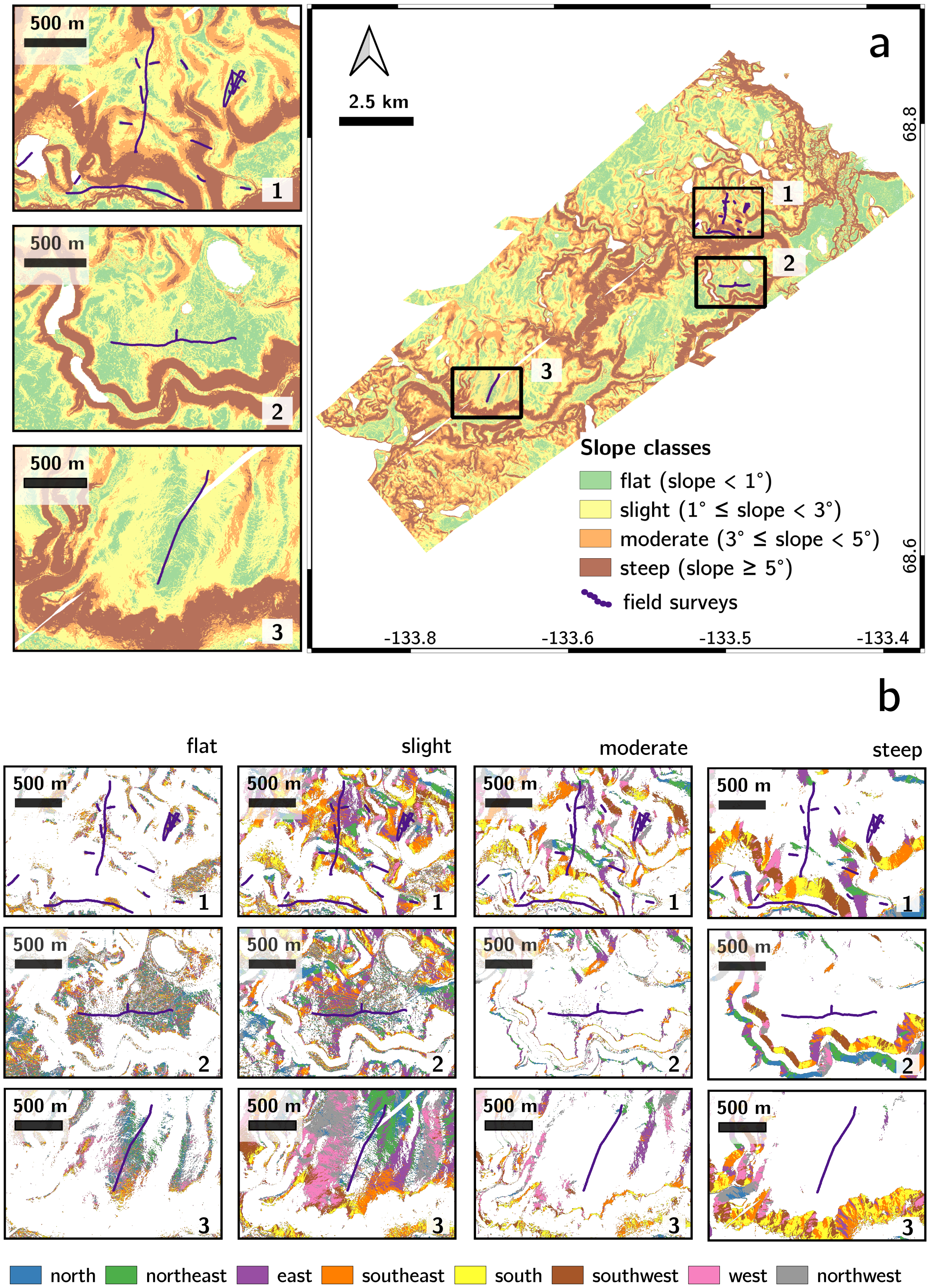

Figure 3.10: Slope and aspect classification. (a) Slope map divided in 4 classes flat (green), slight (yellow), moderate (orange) and steep (brown). As reference, the field snow depth survey locations from March 2023 (Rutter, 2023; Walker, 2023) are shown in purple, and detailed in the insets 1, 2, and 3. In (b), the field survey regions (insets 1, 2, and 3), are separated by slope classes and segmented by cardinal directions (north, northeast, east, southeast, south, southwest, west, northwest). White portions in (b) indicate areas within the inset that have no correspondence within the given slope class, but in one of the neighboring categories.

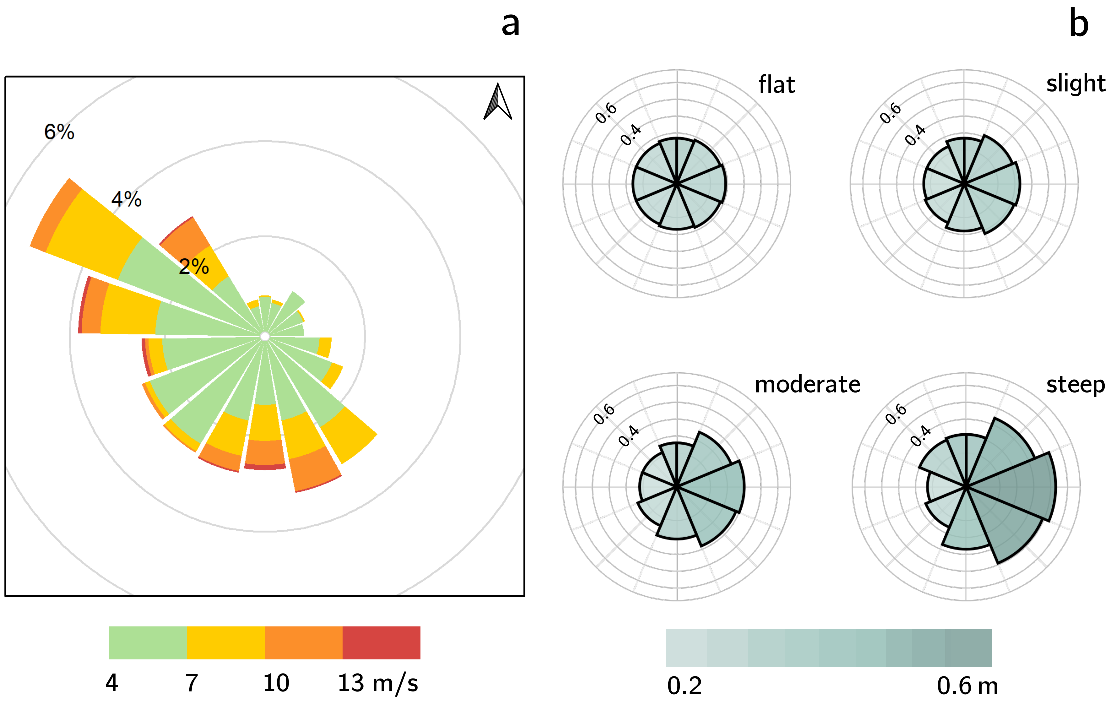

Figure 3.11: Windrose and snow depth across slopes and aspects: In (a), the windrose diagram illustrates prevailing wind directions from October 2022 to April 2023, with hourly records data from wind speeds greater than $4\,\mathrm{m\,s^{-1}}$ (Government of Canada, Environment and Natural Resources, 2024). In (b), the snow depth distribution divided by slope range (from flat to steep), and their corresponding aspect.

showed a broader spread, particularly on moderate slopes facing northeast, east, and southwest, where LiDAR recorded a wider range of values than field measurements (Figure 3.13).

Bias between field and LiDAR measurements was relatively consistent across aspects in flat areas, ranging from 0.17 m to 0.21 m. However, this bias increased with slope steepness, becoming highly dependent on aspect in steeper slopes. For instance, the median difference was as low as 0.11 m on steep north-facing slopes but reached 0.37 m on steep southeast-facing slopes, indicating a significant aspect-related variation in LiDAR underestimation. However, due to limited sample size and uneven aspect coverage in steep areas, conclusions about LiDAR-field measurement relationships in steep regions should be interpreted cautiously.

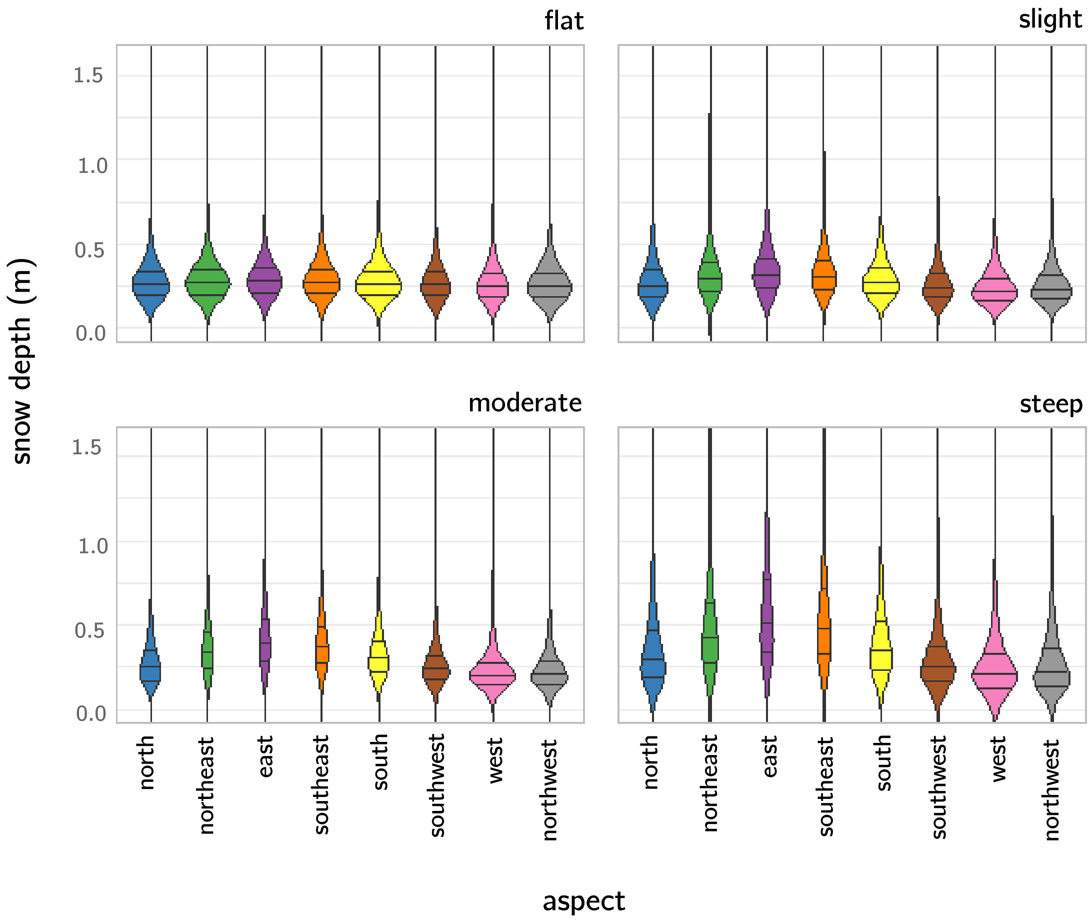

Figure 3.12: Snow depth distribution across slope and aspect classes: This violin plot displays the distribution of the central 99% of LiDAR snow depth data for each slope range (flat, slight, moderate, and steep), with snow depth (m) shown on the y-axis. Within each slope range, snow depth values are grouped by aspect. Each violin represents the density curve of snow depth values, with internal lines marking the median and quartiles.

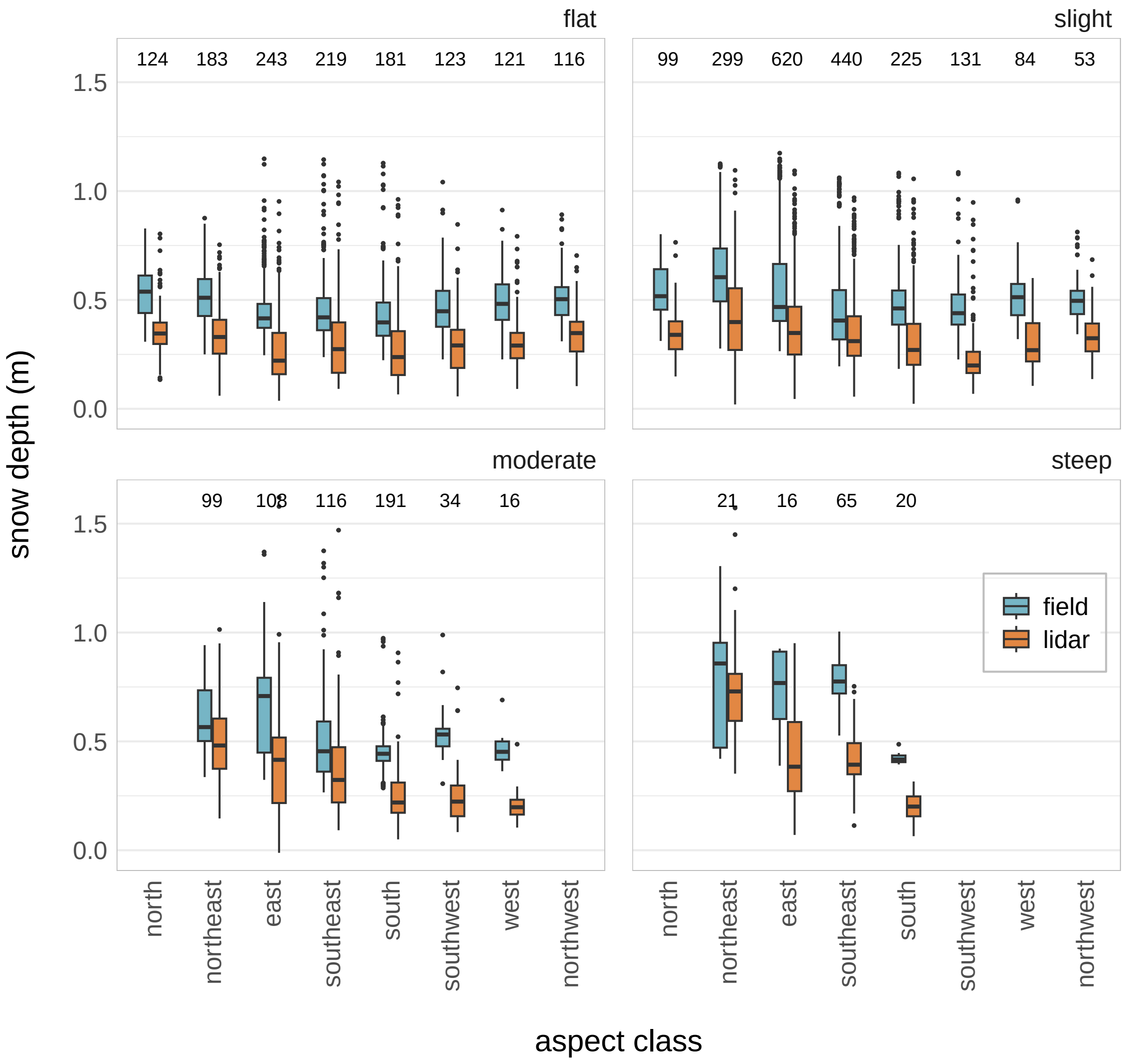

Figure 3.13: Pairwise LiDAR and field measurements across slope and aspect classes: Comparison of LiDAR (orange) and field (blue) snow depth measurements across slope ranges (flat, slight, moderate, and steep), and within each range, their aspect class. Snow depth (m) is shown on the y-axis, with each pair of boxplots representing the depth distribution for each aspect class. Sample sizes are indicated above each pair; classes with fewer than 10 measurements were excluded from the plot.

3.3 Snow depth and vegetation

In order to assess the influence of vegetation on snow depth distribution in Trail Valley Creek, I examined two factors: vegetation height and vegetation cover. Vegetation height was classified into four height ranges, while a 12-class vegetation map was used to differentiate vegetation types. I compared those features with LiDAR snow depth measurements and investigated the relationship between vegetation height and cover with snow depth associated to them. In the sequence, to assess potential biases associated to vegetation cover, I compared field measurements with LiDAR values according to the vegetation height and class categories.

3.3.1 Vegetation height

Approximately 95% of the study area was covered by vegetation under 0.5 m in height, with 64 km^2 occupied by vegetation shorter than 0.1 m and 55 km^2 by vegetation between 0.1 and 0.5 m. Taller vegetation, from 0.5 to over 1.5 m, covered smaller proportions of the area, at 6.6 km^2 and 2.4 km^2, respectively. The focus of this analysis was to explore how snow depth patterns varied with vegetation height and how LiDAR measurements might be affected by these vegetation structures.

Snow depth increased with vegetation height across the study area. The median snow depth ranged from 0.29 m in areas with vegetation under 0.1 m to 0.54 m in areas where vegetation exceeded 1.5 m (Figure 3.14). Similarly, variability in snow depth rose with vegetation height, as reflected by the increasing interquartile ranges and standard deviations, which ranged from 0.19 to 0.45 m, indicating that snow depths were more dispersed in areas with taller vegetation. The skewness and kurtosis values indicated positive skewness across all vegetation height classes, though skewness decreased with taller vegetation. Vegetation under 0.1 m had a skewness of 3.32, reflecting a right-skewed distribution with more lower snow depths and fewer higher extremes. The violin plots show broader distributions for taller vegetation classes above 0.5 m, reflecting the rising interquartile ranges and standard deviations together with vegetation height. The decrease in skewness and kurtosis in these classes is also consistent with more balanced distributions and fewer extreme values compared to shorter vegetation.

Vegetation height and field surveys

While the LiDAR snow depth distribution consistently increased with vegetation height, the field survey sample did not follow the same trend. Pairwise comparisons between field and LiDAR snow depths showed an increase with vegetation height for classes up to 1.5 m, but decreased in the tallest vegetation category (Figure 3.15). Besides that, the correlation coefficient remained fairly consistent across the lower vegetation classes, but dropped significantly for the tallest vegetation, indicating a weaker relationship between the methods in this category. The coefficients for vegetation under 0.1 m, 0.1 to 0.5 m, and 0.5 to 1.5 m were 0.74, 0.75, and 0.81, respectively, deviating only slightly from the unclassified LiDAR and field survey

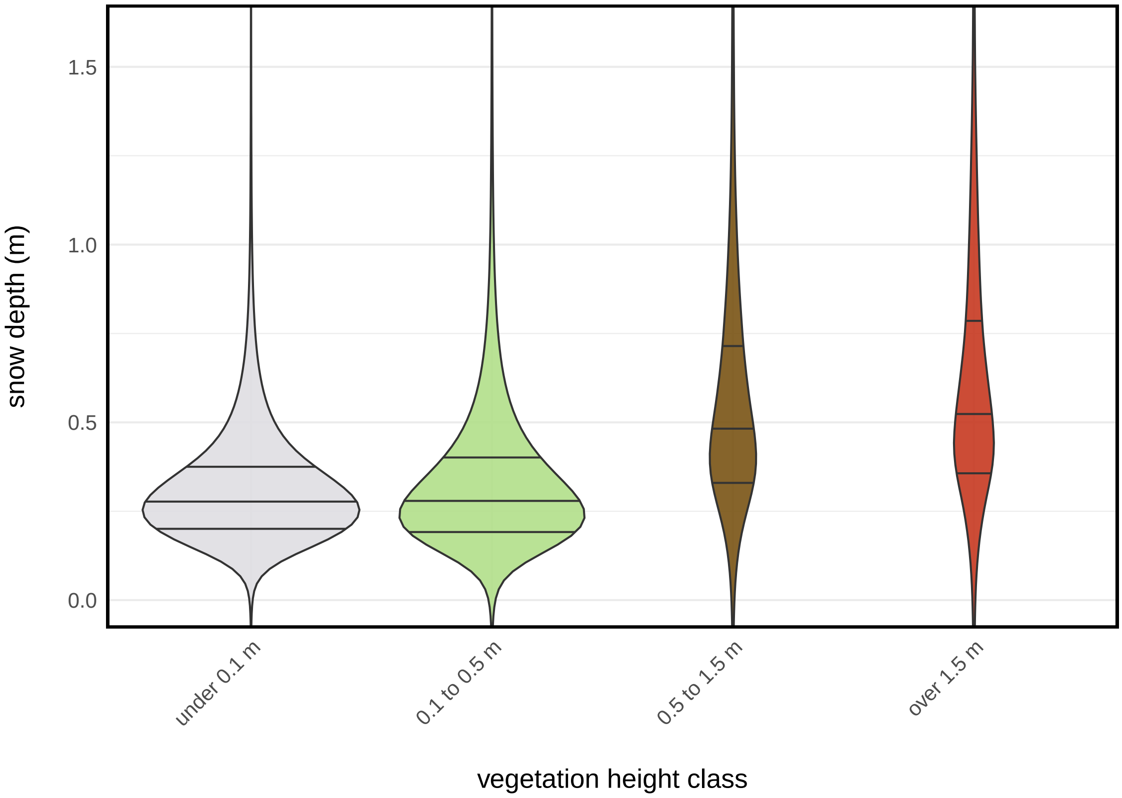

Figure 3.14: Snow depth distribution across vegetation height classes: This violin plot displays the distribution of the central 99% of the LiDAR snow depth data for each vegetation height class, with snow depth (m) on the y-axis. Each violin shows the density curve of the snow depth values, with the internal lines marking the corresponding median and quartiles.

correlation of 0.79. However, for vegetation over 1.5 m, the correlation dropped to 0.38, reflecting the poorest agreement between the two methods in this class.

The median of differences between LiDAR and field measurements also increased with vegetation height, revealing a greater bias in taller vegetation classes. The interquartile range remained similar for both field and LiDAR measurements in vegetation shorter than 0.5 m (around 0.19 m) but increased significantly in the 0.5 to 1.5 m range, reaching 0.27 m for field measurements and 0.37 m for LiDAR, reflecting greater spread and a larger bias. In the tallest vegetation class, the interquartile range decreased again, with values of 0.13 m for field measurements and 0.15 m for LiDAR, indicating closer agreement in the variability, despite the low correlation coefficient and high bias.

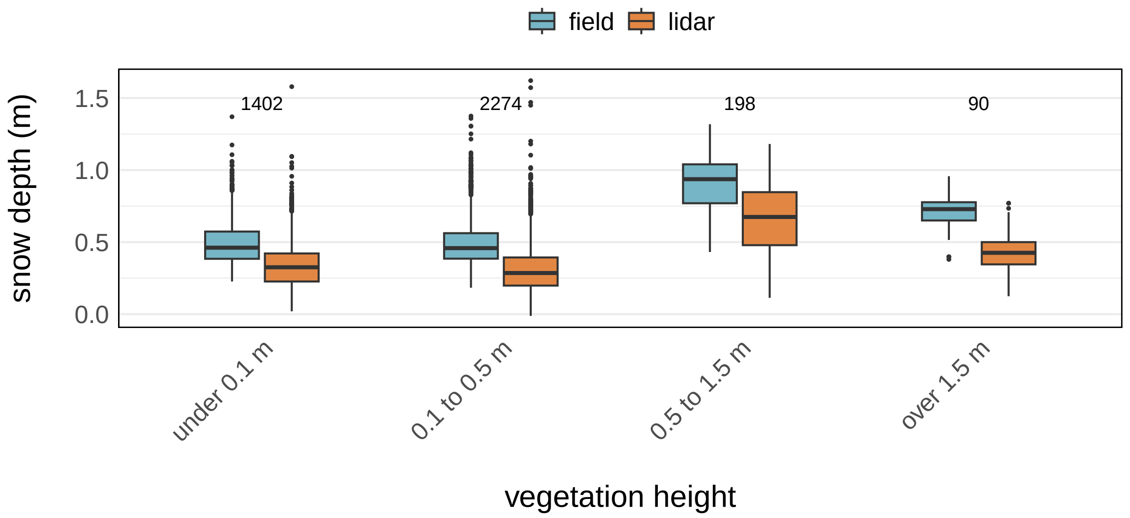

Figure 3.15: Pairwise LiDAR and field measurements across vegetation heights: Comparison of LiDAR (orange) and field (blue) snow depth measurements across vegetation height classes. Snow depth (m) is shown on the y-axis, with each pair of boxplots representing the depth distribution for each vegetation height range. Sample sizes are indicated above each pair.

3.3.2 Vegetation classes

Following the patterns of vegetation height, I also examined the role of vegetation cover in the snow depth distribution of Trail Valley Creek. For this, I used a vegetation class map that classified Trail Valley Creek's land cover into 12 classes, followed by an analysis of the relationship between these classes and biases in LiDAR and field survey measurements.

The area distribution across vegetation classes revealed that dry hummock and dwarf shrub dominate the study area, covering approximately 36.3 km^2 (28.4%) and 34.2 km^2 (26.7%), respectively. Moss and lichen accounted for 14.3 km^2 (11.2%) and 13.4 km^2 (10.5%), while tussock covered around 9.5 km^2 (7.4%). The remaining classes, including baresoil, tree, river, and polygon wet, made up smaller portions of the area, contributing less than 3% of the total area combined.

The LiDAR snow depth distribution showed variation across the 12 vegetation and land cover classes, with river and baresoil having the highest median snow depths (0.64 m and 0.43 m respectively). Although both classes present similar interquartile ranges, baresoil exhibits higher variability, as reflected in its larger standard deviation (0.51 m compared to 0.41 m for river), even with a lower median. The wide spread of values is highly influenced by the lower snow depths, as demonstrated in Figure 3.16.

Following these, single shrub, riparian shrub, and tree classes had the next highest median snow depths, from 0.46 to 0.49 m, with interquartile ranges between 0.33 and 0.39 m, respectively, suggesting a trend of high snow depths associated with taller vegetation. Among the shrubs, the dwarf shrub class exhibited a narrower interquartile range of (0.21 m), yet with heavier tails toward higher snow depths, as indicated by the skewness (3.09) and kurtosis (20.36). Tree areas, on the other hand, exhibited a relatively uniform snow depth distribution when compared to shrubs, with a more symmetrical spread around the median and less overall variability in snow accumulation. Finally, at the lower end of the LiDAR snow depth distribution, polygon dry and tussock classes had the lowest median snow depths, at 0.26 m and 0.25 m, respectively. These classes also exhibited the narrowest interquartile ranges, with polygon dry at 0.12 m and tussock at 0.13 m.

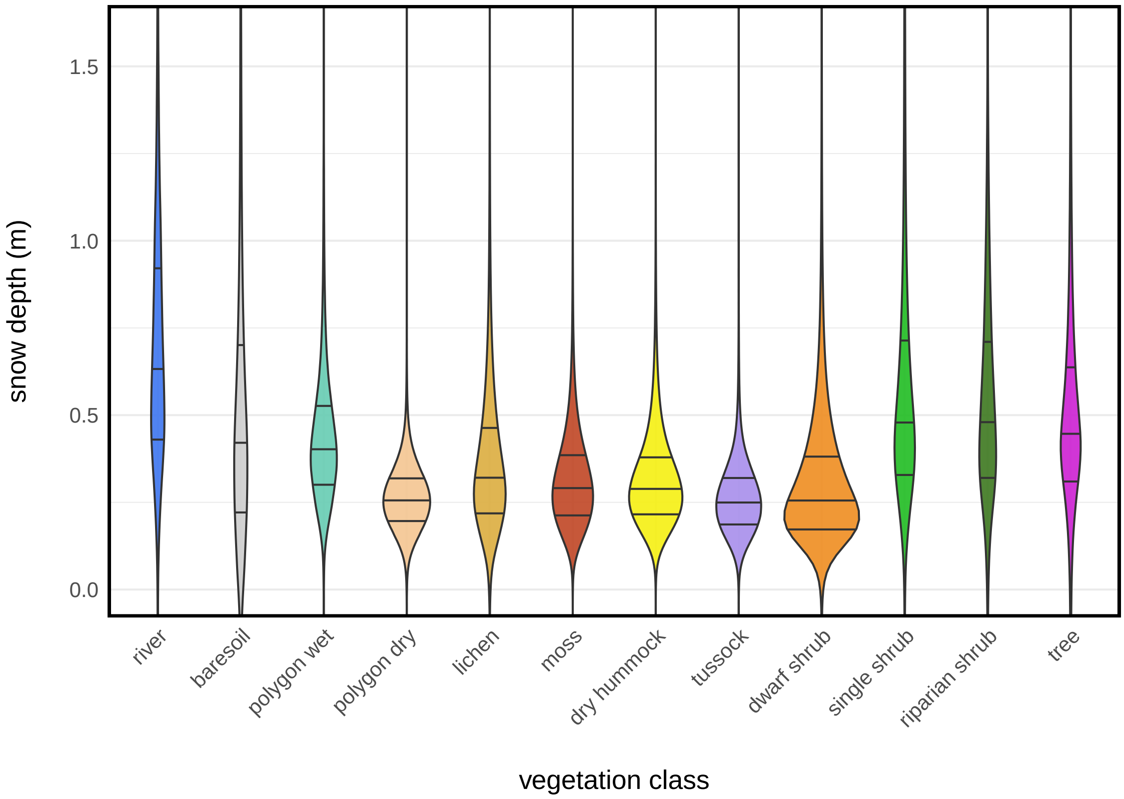

Figure 3.16: Snow depth distribution across vegetation classes: This violin plot displays the distribution of the central 99% of the LiDAR snow depth data for each vegetation class, with snow depth (m) on the y-axis. Each violin shows the density curve of the snow depth values, with the internal lines marking the corresponding median and quartiles.

Vegetation classes and field surveys

The field surveys did not represent the variety of classes in the vegetation map. Baresoil and polygon wet did not meet the minimum sample size of 10, defined as a threshold, were not represented along the remaining classes in the plot.

Tree areas showed the largest biases, with a median of differences of 0.3 m, followed by shrub classes, with median of differences ranging from 0.22 m to 0.25 m. In contrast, lichen and dry hummock showed the smallest discrepancies among methods, both at 0.12 m. The median of differences for tussock and moss, both at 0.19 m, were in line with the general unclassified LiDAR and field survey comparison (Figure 3.17).

Classes like lichen, moss, and dwarf shrub (r = 0.74, 0.75, and 0.82, respectively) showed higher correlations, suggesting that despite varying biases, LiDAR still captured the overall patterns of snow distribution. In contrast, areas with taller or denser vegetation, like trees (r = 0.19) and riparian shrubs (r = 0.63), presented lower correlations. Interquartile ranges and standard deviations further highlighted the variability in snow depths. For instance, single- and riparian shrubs had wider spreads in LiDAR measurements when compared to field values, indicating more variability of snow depths captured by LiDAR in those areas. Classes such as dwarf- and single shrub, had not only lower medians, but also extended to extremely low values, as evidenced by the longer whiskers at the lower end of their LiDAR boxplots.

Additionally, dry hummocks, tussocks, and dwarf shrubs exhibited a high number of outliers in both methods, suggesting the presence of localized areas with higher snow depths. These outliers indicate natural variability in snow accumulation through the landscape, rather than a discrepancy between the two measurement methods. The correlation coefficients in these classes suggest that, despite the variability, both methods captured similar overall patterns in snow distribution.

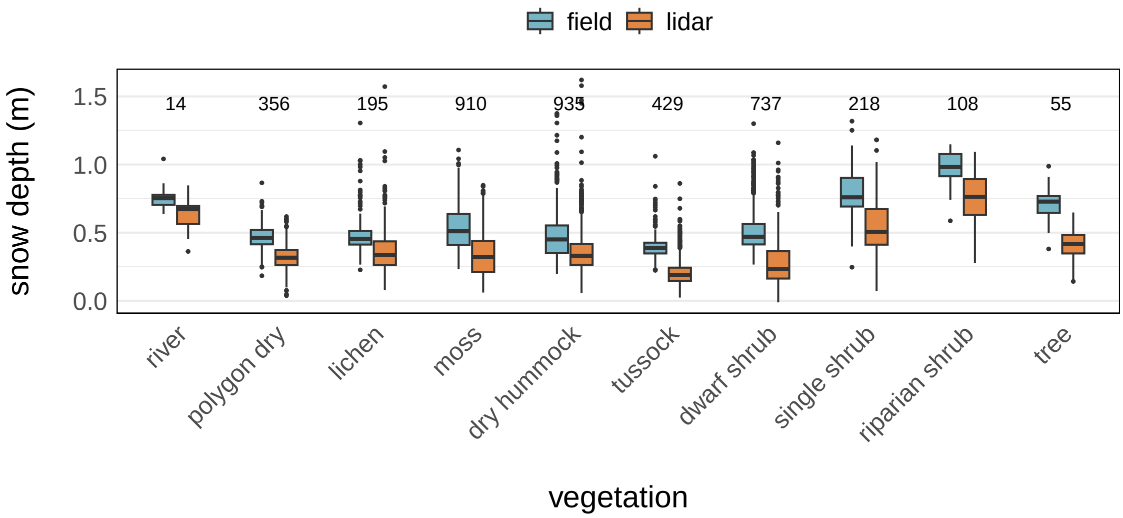

Figure 3.17: Pairwise LiDAR and field measurements across vegetation classes: Comparison of LiDAR (orange) and field (blue) snow depth measurements across vegetation classes. Snow depth (m) is shown on the y-axis, with each pair of boxplots representing the depth distribution for each vegetation class. Sample sizes are indicated above each pair.

Discussion

4.1 Plausibility of snow depth map

4.1.1 LiDAR snow depth map

While the LiDAR snow depth map provides a useful overview of snow distribution, it is important to consider the limitations inherent to the method. Snow depth is dynamic, influenced by wind redistribution, sublimation, melt, and metamorphism (Essery et al., 1999), so the conditions captured over one survey reflect the snow depth distribution at a specific point in time. Although these data do not capture the evolution of snow cover throughout the winter and cannot be extrapolated to other years, the high-resolution snow depth map provides valuable insight into the relationships between snow distribution, geomorphology, and vegetation cover. Across most of the 127 km^2 mapped area in Trail Valley Creek, snow depth values—representing the central 99% of the data—ranged from 0.00 m to 1.60 m, with half of the area exhibiting depths between 0.21 m and 0.42 m. At the lower end, negative values accounted for 0.49% of the dataset, covering about 634 377 m^2, while the uppermost 0.5%, spanning 638 530 m^2, ranged from 1.60 m to a maximum of 8.15 m.

Both the winter and summer LiDAR campaigns that provided the snow depth estimations for this study took place within the same year. This has potentially helped minimize errors in snow depth estimates that could arise from elevation discrepancies due to terrain erosion or vegetation cover changes. Although these processes are typically subtle over short periods, land cover changes such as the opening of the ITH, in November 2017, can have a local measurable impact within a short time span. For instance, the comparison between AWI's digital terrain model from the summer 2018 (Lange et al., 2021) and summer 2023, used in this work, shows that the road has subsided by tens of centimeters within a 5-year period.

Errors can also arise during the processing of LiDAR data, particularly through the misclassification of landscape features. The simple morphological filter (SMRF) method, introduced by Pingel et al. (2013), uses both the first and last returns of the point cloud to classify points as either bare earth (in this case, the snow surface) or objects. Although the last return is more likely to represent the surface, it is not always the case, which can lead to two types of classification errors: Type I errors, where bare earth points are mistakenly classified as objects, and Type II errors, where objects are incorrectly classified as bare earth points. Pingel et al.

(2013) found that moderate and steep slopes tend to exhibit more Type II errors, meaning that objects are more frequently misclassified as bare earth in these areas. This misclassification can artificially raise surface elevations, potentially inflating snow depth estimates at these points. Despite these challenges, the smoothness and high reflectivity of snowpacks generally allow for greater accuracy in LiDAR measurements of snow-covered surfaces compared to snow-free terrain (Hopkinson et al., 2012).

In addition, discrepancies can also arise from the horizontal alignment between snow-free and snow-covered terrain. Digital elevation models from two different seasons must be resampled and aligned to ensure that each pixel matches the exact position of its corresponding pixel before calculating snow depth. This slight adjustment and repositioning can cause more pronounced discrepancies over steep slopes, where small misalignments are amplified due to the slope gradient. Misalignments can also affect measurements over sparse trees or shrubs as slight offsets may cause the LiDAR to capture different parts of the structure in each season. Furthermore, vertical errors are also a potential issue (Hopkinson et al., 2004) that can add to the overall uncertainty of a LiDAR map.

Aiming to minimize vertical errors, standardize the merge of multiple elevation rasters, and avoid abrupt elevation changes at the edges of flight rounds (artifacts), I vertically adjusted the parallel flight-round rasters using an intersecting flight round as a benchmark to calculate the offsets. The resulting offsets, ranging from -0.05 to 0.01 m, helped to standardize the data by leveling them using a common parameter. As part of the post-processing choices, I also decided to exclude snow depth measurements over water bodies, since the LiDAR data in these areas was unreliable, as demonstrated by Skaugen and Melvold (2019). However, in contrast to their approach, I retained negative snow depth values to avoid masking potential patterns arising from the laser scanning or data processing.

Besides the potential errors of snow-free and snow-covered terrain digital elevation models and subsequently the snow depth estimations, the spatial accuracy of field measurements, which can range from 3 to 10 m (Sturm and Holmgren, 2018; Walker et al., 2020), introduces another source of variability. By averaging the field measurements with a 5-m buffer, I aimed to mitigate these discrepancies and bring the LiDAR and field survey datasets into better alignment. Additionally, although field snow depths were measured in different days, I assumed minimal snow redistribution or changes during this period given the short period of time between the surveys, and combined the field measurements into a single dataset without adjusting for collection dates.

The comparison of snow depth measurements between the ITH and field surveys provided valuable insights into snow distribution patterns across varying landscapes. While the highway served as a stable, low-variability reference point, with minimal influence from topography or vegetation, the field measurements captured snow depths over more complex terrain with diverse slopes and vegetation structures. These differences highlighted the challenges of snow depth estimation in natural settings, pose challenges for precise snow depth estimation.

4.1.2 Snow depth and the ITH

The construction and maintenance of the ITH have had a measurable impact on snow distribution patterns in Trail Valley Creek. Regular plowing operations ensure the road remains clear of snow, while depositing snow along the embankments, causing increased snow accumulation up to 36 m from the road center (Hammar et al., 2023). As the road is regularly cleared, I used its midpoint as a parameter for negligible snow depth, as benchmark to assess the performance of the snow depth map.

The LiDAR snow depths along the control points on the ITH aligned well with the expected zero reference, with both the mean and median snow depths under 0.02 m, and an interquartile range around0.07 m. The data follows an approximately normal distribution, with a slight positive skew, further supporting the accuracy of the LiDAR product. The road served as a consistent reference parameter due to its homogeneity: it is constituted from the same material, which maintains consistency in the spectral response, and lacks the terrain roughness and complexity of vegetated areas. The accuracy also suggests negligible changes in elevation between the seasons due to settlement or potential seasonal volume changes.

4.1.3 Field surveys

Field snow depth measurements were generally higher than those from LiDAR, which agrees with the literature (Berezovskaya and Kane, 2007; Hopkinson et al., 2004, 2012; Walker et al., 2020). In 93% of the 3,964 field points, field measurements exceeded LiDAR depths, with a median difference of 0.17 m between the two methods. Berezovskaya and Kane (2007) attributed this overestimation in field measurements to the probe penetrating beyond the snow-ground boundary, sometimes reaching the unfrozen organic layer. Additionally, LiDAR often underestimates snow depth due to ground-level vegetation misclassifications, where the digital terrain model may misinterpret vegetation as bare ground (Hopkinson et al., 2012), artificially elevating the base level. Although the LiDAR values were higher than the field surveys, both methods had very similar standard deviations (0.19 m), interquartile ranges (0.21 m), and had a correlation coefficient of 0,79, showing that both methods agreed well despite bias. LiDAR snow depths also showed a wider range, capturing extreme values, including negative snow depths, due to variations in surface detection, terrain heterogeneity, and data alignment.

4.2 Influence of topography on snow depth distribution

Arctic regions, characterized by vast open spaces and limited freeze-melt cycles or rain-on-snow events, are especially susceptible to snow redistribution by wind (Pohl and Marsh, 2006). This interaction of wind and terrain, combined with the Arctic's irregular landscape, underscores topography as a primary factor in snow distribution (Pomeroy et al., 1997). In Trail Valley Creek, this influence of topography was evident: landform, slope, and aspect classifications together highlighted the role of geomorphology in snow depth distribution, with each layer contributing distinct details to the analysis.

The geomorphons approach (Jasiewicz and Stepinski, 2013) classified the snow-free digital terrain model into landforms based on terrain shape, with the output determined by key parameters that must be actively selected, like the slope threshold. In Trail Valley Creek's relatively flat terrain (Pohl and Marsh, 2006), I set the slope threshold to 2 degrees to capture subtle elevation changes, as increasing this threshold would simplify the landscape into broader flat areas, as demonstrated on Figure 2.4. While the landform classification allows for some flexibility in defining terrain features, slope and aspect classifications are strictly defined by degree and direction, systematic measures which can provide insights into snow transport and wind-driven redistribution.

Snow depths increased with slope steepness, with northeast, east, and southeast-facing slopes consistently showing higher snow depths across all slope classes. While topography showed a clear association with snow depth, wind patterns further revealed that snow accumulation aligned closely with prevailing wind directions. According to Li and Pomeroy (1997), winds above 4 m/s are sufficient to transport dry snow, while wet snow requires speeds over 7 m/s. Hourly records from the Trail Valley weather station during Winter 2022-2023 showed that winds above this 4 m/s threshold predominantly came from the west and northwest, aligning with higher snow depths in the northeast, east, and southeast, and lower depths on west and southwest-facing slopes (Government of Canada, Environment and Natural Resources, 2024). Although aspect influenced snow depths across all slope categories, its effect was more pronounced on moderate and steep slopes than on flatter areas.

Higher slopes also showed more outliers and negative snow depths. This could indicate systematic errors commonly associated with steep terrain, such as angle of incidence between the laser pulse and the ground surface, shadowing, and reduced point density in comparison to flat areas. This trend is consistent with findings from Hopkinson et al. (2012), who observed increased LiDAR outliers and higher standard deviations on steep slopes and in gullies. Similarly, the dataset used in this work, standard deviations were higher over slopes, footslopes, and valleys, increasing with slope gradient. When analysing the median snow depths by landform, slopes, footslopes, and valleys showed the highest records, contrasting with the shallow snow on ridges. This pattern is expected, as low-lying areas retain more snow due to reduced wind exposure, while ridges experience greater wind-driven redistribution.

Field measurements consistently showed higher snow depths than LiDAR across all landforms and slope classes. The median difference between field and LiDAR measurements ranged from 0.17 m in flat areas to 0.29 m on steep slopes, where correlation also dropped sharply ($r = 0.62$), indicating greater discrepancies on steeper terrain. With 80% of samples collected from flat and slight slope areas, steep slopes were underrepresented, impacting statistical robustness in these regions. Aspect added another layer to these observations: in flat and slight slopes, field and LiDAR measurements showed similar variability across all aspects. However, in moderate slopes, LiDAR values displayed a broader distribution, particularly on northeast, east, and southwest-facing slopes, consistent with the general LiDAR snow depth distribution. Bias remained steady in flat areas but became increasingly aspect-dependent on steeper slopes, with median differences ranging from 0.11 m on north-facing slopes to 0.37 m on southeast-facing slopes. Yet, the limited sample size and uneven aspect coverage in steep areas suggest caution in interpreting these patterns as definitive relationships between LiDAR and field measurements.

Although landform and slope maps each provide unique insights into landscape geomorphology, some classes overlap, such as the ‘flat’ and ‘slight’ slopes and the ‘flat’ landform class. These overlapping areas (Figures 3.7 and 3.10) show similar snow depth means, medians, and standard deviations. Consistent with the slope context, the 'flat' landform had the lowest bias among landforms when compared to field surveys, with a median underestimation of 0.14 m, while ridges had the largest bias of 0.24 m. Shoulders and footslopes also showed large median differences but maintained high correlation coefficients and similar standard deviations between field and LiDAR values, indicating that these landforms, despite bias, show consistent variability and agreement between measurement methods.

4.3 Influence of vegetation on snow depth distribution

Although counterintuitive, negative snow depths can occur because they result from subtracting two elevation datasets—snow-free and snow-covered. This happens when a pixel in the snow-free dataset has a higher elevation than in the snow-covered one, often due to slight misalignments or differences in the structures captured by the LiDAR. For instance, sparse vegetation, such as single shrubs or trees, can lead to variations in the detected elevation depending on which parts of the vegetation are captured by the LiDAR within the laser point density. For example, depending on the point density and alignment, the LiDAR could detect the top of a shrub in one dataset and the ground beside it in another, leading to discrepancies in elevation that can produce negative snow depth values. Conversely, if a LiDAR point in winter measures the top of a tree protruding above the snowpack while the summer DTM correctly captures the ground level, the calculated snow depth at this pixel will be artificially elevated, resulting in values significantly higher than actual snow depths. LiDAR point density can also impact the estimation of vegetation height. The aerial laser scanning flight paths are planned with overlapping margins, creating areas with higher point density. This increased density captures more details of vegetation structures, resulting in a noticeable stripe pattern on the vegetation height map (Figure 2.5). In these overlapped areas, vegetation heights appear elevated relative to adjacent, non-overlapping areas, creating abrupt transitions parallel to the flight paths. These abrupt transitions are artifacts of data collection rather than true landscape features, which suggests that vegetation height could appear underestimated in regions with lower point density.

As reported by Hopkinson et al. (2004), the presence of dense vegetation, particularly in deciduous forests, can exacerbate LiDAR measurement discrepancies, leading to even greater inaccuracies as canopy interfere with LiDAR's ability to accurately detect the ground surface. For this reason, some studies, like that of Dai et al. (2024), choose to selectively avoid dense vegetation areas to simplify digital elevation models. My data showed that LiDAR had the lowest correlation with field data in areas with the tallest vegetation and tree cover, where agreement was poorest and biases highest, confirming the highest LiDAR underestimation in these regions.

Vegetation height and vegetation classes exhibited similar effects on snow depth distribution, with snow depths increasing alongside vegetation height, as shown by higher mean, median, standard deviation, and interquartile range values. This pattern reflects the established understanding that taller vegetation tends to trap more snow due to greater surface area and structural complexity, which can reduce wind speed and limit snow dispersion (Shirley et al., 2023). Among vegetation types, taller shrubs and trees displayed the greatest snow depths. Wilcox et al. (2019) demonstrated that deeper snow over tall alder shrub areas, compared to dwarf shrub areas, results in delayed snowmelt. However, if these taller shrubs protrude above the snowpack, they can reduce local albedo and accelerate snowmelt, a critical consideration in regions with lower snow depths (Sturm et al., 2001; Wilcox et al., 2019). This suggests that in scenarios of increased shrubification and reduced snowfall, albedo effects might counteract snow-trapping advantages, potentially leading to earlier melt despite deeper snowpacks (Sturm et al., 2010; Wilcox et al., 2019).

Notably, while vegetation height generally corresponds with snow depth, the highest snow depth overall was observed in the river class. Whereas included in the vegetation map, 'river' represents a structural feature rather than true vegetation class; instead, it aligns with landform-related findings agreeing that valleys tend to accumulate the deepest snow packs.

Although the research questions focused on topography and vegetation separately, the two are closely interconnected. For example, shrubs predominantly grow in valleys due to greater nutrient availability and moisture (Essery and Pomeroy, 2004). Sturm et al. (2001) found that the tallest, densest shrubs—often situated near water tracks and riparian zones—are associated with the deepest snow depths, as the deep snowpacks shield shrubs from cold winter air, desiccation, and abrasion. However, according to Shirley et al. (2023), when shrubs are not confined to topographic lows, they exert a stronger influence on snow depth and local snow redistribution than topography itself. In the same context, polygon wet and dry centers—like the river class—are best interpreted as structural or topographic features, despite being a class in the vegetation map. Polygon wet centers, or low-centered polygons, generally hold water or support short graminoids. The fact that polygon wet centers showed high snow depths might be better explained by their concave structure, rather than by vegetation trapping, as observed by Wainwright et al. (2017). In contrast, polygon dry centers (high-centered polygons), with their convex shape, were associated with some of the lowest snow depths in both the snow depth map and field records.

This relationship between topography, vegetation, and snow depth extends to active layer depth as well. Ridges, which had the lowest snow depths, also correspond to shallower active layers (Grünberg et al., 2020), while areas with taller shrubs, where snow depths are greatest, exhibit deeper active layers. This pattern likely reflects the soil properties in valleys and depressions, where organic matter and nutrients promote vascular plant growth. Thus, while taller shrubs trap more snow, they also benefit from favorable topographic settings that support deeper snowpack development.

While vegetation height and density correlated with snow depth, baresoil areas—despite their broad spread and low to negative values—also showed mean and median snow depths higher than moss, lichen, tussock, and dwarf shrubs, suggesting an influence of topography. As baresoil is uncommon in organic-rich environments like valleys, this pattern may instead relate to slope and aspect.

Although field surveys underrepresented certain classes (steep slopes, as well as baresoil and polygon wet) it captured the distribution trends of LiDAR snow depths in most of the cases and showed valuable data about class-related bias. Field measurements aligned with the general LiDAR distribution, showing similar patterns, including the skewness in lichen, dry hummock, tussock, and dwarf shrubs. Correlation coefficients reveal that the relationship between field and LiDAR measurements weakens as vegetation height increases. For vegetation under 1.5 m, correlation remains strong ($r = 0.74$–0.81), indicating consistent snow distribution between methods. However, in vegetation above 1.5 m, correlation drops to 0.38, underscoring LiDAR's reduced accuracy in densely vegetated or forested areas.

Conclusion

The results demonstrated that field survey consistently report higher snow depths than LiDAR measurements, with LiDAR generally underestimating depths across all the studied vegetation and topographic settings. Despite this consistent underestimation, LiDAR measurements align closely with field survey distributions, often with similar interquartile ranges, though shifted towards lower values. Agreement is strongest over flatter slopes and areas with shorter vegetation, and diminishes in complex landscapes with steep slopes, taller and denser vegetation, where biases are also highest.

Snow accumulation patterns correspond with both topographic and vegetation features, showing deeper snow in micro- and macrotopographic lows, such as polygon wet centers and valleys, on leeward sides of steeper slopes, and in areas with taller vegetation. An intricate relationship exists between topography and vegetation, as taller vegetation can trap snow, while its growth is also favored in topographic lows where wind abrasion is lower and nutrient availability is greater.

The study revealed significant snow depth variation among slope aspects, with highest depths recorded on northeast, east and southeast aspects of steep slopes, consistent with predominant wind patterns from the west and northweast at speeds above $4\,\mathrm{m\,s^{-1}}$. Lastly, LiDAR measurements over the ITH section intersecting the area of interest showed a snow depth median of $0.017\,\mathrm{m}$, demonstrating high accuracy over homogeneous, non-natural terrain.

This study is the first to utilize this combination of datasets to examine snow depth distribution across varied landforms, slopes, aspects, and vegetation types in Trail Valley Creek. The extensive area coverage and high resolution make this dataset a useful starting point for future research, including analyses of outlier patterns in LiDAR snow depths and more detailed statistical investigation of spatial relationships within the snow cover.

Acknowledgement

I would like to thank my supervisors, Professor Julia Boike and Inge Grünberg, for always being so kind, for teaching and guiding me throughout this thesis, and above all, for never giving up on me. I would also like to thank Nick Rutter and Branden Walker for kindly providing their field survey measurement data, without which half of this work wouldn't have been possible.
I want to thank the SPARC thesis discussion team, who have been disentangling all the knots with me and helping me organize the chaos in my head into coherent lines of thought: Marie Rolf, Jannika Gottuk, Luisa Näke, Maybrit Goldau, Laura Becker, and Jael Mencke. My thanks also go to the entire SPARC group in Potsdam, and to Jennika Hammar for envisioning this Master's thesis with me and introducing me to the world of digital elevation models.
I would like to thank my comrades at the Humboldt University of Berlin—Maeve, Camila, Issi, Ellfie, Liang, Yuki, Benni, Melanie, Thamires, and Livia—who were there before and after the pandemic. And to everyone who took—and continues to take—their time to upload tutorials on the internet: you are all part of this.
Finally, I would like to thank my family, and Kai and Moema, for all their love and moral support throughout all the ups and downs of this journey.
Lots of love and data to you all.
Thanks a lot.

Bibliography

Aalstad, K., Westermann, S., and Bertino, L.: Evaluating satellite retrieved fractional snow-covered area at a high-Arctic site using terrestrial photography, Remote Sensing of Environment, 239, 111 618, https://doi.org/https://doi.org/10.1016/j.rse.2019.111618, URL https://www.sciencedirect.com/science/article/pii/S0034425719306388, 2020.

AHRG: Trail Valley Creek Arctic Research Station, URL https://www.trailvalleycreek.ca/about(Accessed:28.06.2023).

Anders, K., Antonova, S., Boike, J., Gehrmann, M., Hartmann, J., Helm, V., Höfle, B., Marsh, P., Marx, S., and Sachs, T.: Airborne laser scanning (ALS) point clouds of Trail Valley Creek, NWT, Canada (2016), PANGAEA, https://doi.org/10.1594/PANGAEA.894884, 2018.

Antonova, S., Thiel, C., Höfle, B., Anders, K., Helm, V., Zwieback, S., Marx, S., and Boike, J.: Estimating tree height from TanDEM-X data at the northwestern Canadian treeline, Remote Sensing of Environment, 231, 111 251, https://doi.org/10.1016/j.rse.2019.111251, 2019.

AWI: Digital terrain model of Trail Valley Creek from 2023, unpublished work, 2024a.

AWI: Vegetation height map of Trail Valley Creek, unpublished work, 2024b.

AWI, A. W. I.: IceBird Project, https://www.awi.de/en/science/climate-sciences/sea-ice-physics/projects/ice-bird.html, retrieved on July 7, 2024, 2024c.

Beamish, A., Raynolds, M. K., Epstein, H., Frost, G. V., Macander, M. J., Bergstedt, H., Bartsch, A., Kruse, S., Miles, V., Tanis, C. M., et al.: Recent trends and remaining challenges for optical remote sensing of Arctic tundra vegetation: A review and outlook, Remote Sensing of Environment, 246, 111 872, https://doi.org/10.1016/j.rse.2020.111872, 2020.

Berezovskaya, S. and Kane, D. L.: Measuring snow water equivalent for hydrological applications: part 1, accuracy of observations, in: Proceedings of the 16 th International Northern Research Basins Symposium and Workshop, Petrozavodsk, Russia, pp. 29–37, 2007.

Berner, L. T., Massey, R., Jantz, P., Forbes, B. C., Macias-Fauria, M., Myers-Smith, I., Kumpula, T., Gauthier, G., Andreu-Hayles, L., Gaglioti, B. V., et al.: Summer warming explains widespread but not uniform greening in the Arctic tundra biome, Nature Communications, 11, 4621, https://doi.org/https://doi.org/10.1038/s41467-020-18479-5, 2020.

Biskaborn, B. K., Smith, S. L., Noetzli, J., Matthes, H., Vieira, G., Streletskiy, D. A., Schoeneich, P., Romanovsky, V. E., Lewkowicz, A. G., Abramov, A., et al.: Permafrost is warming at a global scale, Nature communications, 10, 264, 2019.

Callaghan, T. V., Johansson, M., Brown, R. D., Groisman, P. Y., Labba, N., Radionov, V., Barry, R. G., Bulygina, O. N., Essery, R. L., Frolov, D., et al.: The changing face of Arctic snow cover: A synthesis of observed and projected changes, Ambio, 40, 17–31, https://doi.org/10.1007/s13280-011-0212-y, 2011a.

Callaghan, T. V., Johansson, M., Brown, R. D., Groisman, P. Y., Labba, N., Radionov, V., Bradley, R. S., Blangy, S., Bulygina, O. N., Christensen, T. R., et al.: Multiple effects of changes in Arctic snow cover, Ambio, 40, 32–45, https://doi.org/10.1007/s13280-011-0213-x, 2011b.

Chadburn, S., Burke, E., Cox, P., Friedlingstein, P., Hugelius, G., and Westermann, S.: An observation-based constraint on permafrost loss as a function of global warming, Nature climate change, 7, 340–344, https://doi.org/10.1038/NCLIMATE3262, 2017.

Dai, C., Howat, I. M., van der Sluijs, J., Liljedahl, A. K., Higman, B., Freymueller, J. T., Ward Jones, M. K., Kokelj, S. V., Boike, J., Walker, B., and Marsh, P.: Applications of ArcticDEM for measuring volcanic dynamics, landslides, retrogressive thaw slumps, snowdrifts, and vegetation heights, Science of Remote Sensing, 9, 100 130, https://doi.org/https://doi.org/10.1016/j.srs.2024.100130, URL `https://www.sciencedirect.com/science/article/pii/S2666017224000142`, 2024.

Deems, J. S., Painter, T. H., and Finnegan, D. C.: Lidar measurement of snow depth: a review, Journal of Glaciology, 59, 467–479, https://doi.org/10.3189/2013JoG12J154, 2013.

Derksen, C., Silis, A., Sturm, M., Holmgren, J., Liston, G. E., Huntington, H., and Solie, D.: Northwest Territories and Nunavut snow characteristics from a subarctic traverse: Implications for passive microwave remote sensing, Journal of Hydrometeorology, 10, 448–463, https://doi.org/10.1175/2008JHM1074.1, 2009.

Dharmadasa, V., Kinnard, C., and Baraër, M.: An accuracy assessment of snow depth measurements in agro-forested environments by UAV lidar, Remote Sensing, 14, 1649, https://doi.org/10.3390/rs14071649, 2022.

Esri, DigitalGlobe, GeoEye, i cubed, FSA, U., USGS, AEX, Getmapping, Aerogrid, IGN, IGP, swisstopo, and the GIS User Community: Esri Satellite Imagery, accessed: 2023-01-02, 2023.

Essery, R. and Pomeroy, J.: Vegetation and topographic control of wind-blown snow distributions in distributed and aggregated simulations for an Arctic tundra basin, Journal of hydrometeorology, 5, 735–744, https://doi.org/10.1175/1525-7541(2004)005⟨0735:VATCOW⟩2.0.CO;2, 2004.

Essery, R., Li, L., and Pomeroy, J.: A distributed model of blowing snow over complex terrain, Hydrological Processes, 13, 2423–2438, https://doi.org/https://doi.org/10.1002/(SICI)1099-1085(199910)13:14/15⟨2423::AID-HYP853⟩3.0.CO;2-U, 1999.

Gouttevin, I., Menegoz, M., Dominé, F., Krinner, G., Koven, C., Ciais, P., Tarnocai, C., and Boike, J.: How the insulating properties of snow affect soil carbon distribution in the continental pan-Arctic area, Journal of Geophysical Research: Biogeosciences, 117, https://doi.org/10.1029/2011JG001916, 2012.

Government of Canada, Environment and Natural Resources: Historical Climate Data. Trail Valley., `https://climate.weather.gc.ca/`, URL `https://climate.weather.gc.ca/`, accessed: 2024-05-16, 2024.

GRASS Development Team: r.geomorphon Documentation, `https://grass.osgeo.org/grass83/manuals/r.geomorphon.html`, accessed: 2024-01-21, 2023.

Grünberg, I. and Boike, J.: Vegetation map of Trail Valley Creek, Northwest Territories, Canada, https://doi.org/10.1594/PANGAEA.904270, URL `https://doi.org/10.1594/PANGAEA.904270`, 2019.

Grünberg, I., Wilcox, E. J., Zwieback, S., Marsh, P., and Boike, J.: Linking tundra vegetation, snow, soil temperature, and permafrost, Biogeosciences, 17, 4261–4279, https://doi.org/10.5194/bg-17-4261-2020, 2020.

Grünberg, I.: Vegetation class map of Trail Valley Creek, unpublished work, 2024.

Hammar, J., Grünberg, I., Hendricks, S., Jutila, A., Helm, V., and Boike, J.: Snow covered digital elevation model and snow depth product (2019), Trail Valley Creek, NWT, Canada, https://doi.org/10.1594/PANGAEA.962552, URL `https://doi.org/10.1594/PANGAEA.962552`, 2023.

Hammar, J., Grünberg, I., Kokelj, S. V., van der Sluijs, J., and Boike, J.: Snow accumulation, albedo and melt patterns following road contruction on permafrost, Inuvik-Tuktoyaktuk Highway, Canada, The Cryosphere Discussions, 17, 1–22, https://doi.org/10.5194/tc-2023-111, URL `https://tc.copernicus.org/preprints/tc-2023-111/`, 2023.

Harder, P., Schirmer, M., Pomeroy, J., and Helgason, W.: Accuracy of snow depth estimation in mountain and prairie environments by an unmanned aerial vehicle, The Cryosphere, 10, 2559–2571, https://doi.org/10.5194/tc-10-2559-2016, URL https://tc.copernicus.org/articles/10/2559/2016/, 2016.

Harris, S., French, H., Heginbottom, J., Johnston, G., Ladanyi, B., et al.: Glossary of Permafrost and Related Ground-Ice Terms, Tech. Rep. Tech. Memo. 142, National Research Council of Canada, Ottawa, Canada, URL https://globalcryospherewatch.org/reference/glossary_docs/permafrost_and_ground_terms_canada.pdf, 1988.

Hopkinson, C., Sitar, M., Chasmer, L., and Treitz, P.: Mapping snowpack depth beneath forest canopies using airborne lidar, Photogrammetric Engineering & Remote Sensing, 70, 323–330, https://doi.org/10.14358/PERS.70.3.323, 2004.

Hopkinson, C., Pietroniro, A., and Pomeroy, J.: HYDROSCAN: Airborne laser mapping of hydrological features and resources, Canadian Water Resources Association, Saskatoon, 2008.

Hopkinson, C., Collins, T., Anderson, A., Pomeroy, J., and Spooner, I.: Spatial snow depth assessment using LiDAR transect samples and public GIS data layers in the Elbow River watershed, Alberta, Canadian Water Resources Journal/Revue canadienne des ressources hydriques, 37, 69–87, https://doi.org/10.4296/cwrj3702893, 2012.

IPCC, I. P. o. C. C.: Polar Regions, p. 203–320, Cambridge University Press, https://doi.org/10.1017/9781009157964.011, URL http://dx.doi.org/10.1017/9781009157964.011, 2022.

Isenburg, M.: ”LAStools - efficient LiDAR processing software”, URL http://rapidlasso.com/LAStools, 2023.

Jasiewicz, J. and Stepinski, T. F.: Geomorphons — a pattern recognition approach to classification and mapping of landforms, Geomorphology, 182, 147–156, https://doi.org/10.1016/j.geomorph.2012.11.005, URL https://www.sciencedirect.com/science/article/pii/S0169555X12005028, 2013.

King, J., Derksen, C., Toose, P., Langlois, A., Larsen, C., Lemmetyinen, J., Marsh, P., Montpetit, B., Roy, A., Rutter, N., and Sturm, M.: The influence of snow microstructure on dual-frequency radar measurements in a tundra environment, Remote Sensing of Environment, 215, 242–254, https://doi.org/https://doi.org/10.1016/j.rse.2018.05.028, URL https://www.sciencedirect.com/science/article/pii/S003442571830258X, 2018.

Krumpen, T., Jutila, A., Coll, C. S., and Horvath, E.: IceBird Winter 2023 Campaign Report, URL https://epic.awi.de/id/eprint/57734/, 2023.

Lange, S., Grünberg, I., Anders, K., Hartmann, J., Helm, V., and Boike, J.: Airborne Laser Scanning (ALS) Point Clouds of Trail Valley Creek, NWT, Canada (2018), https://doi.org/10.1594/PANGAEA.934387, URL https://doi.org/10.1594/PANGAEA.934387, 2021.

Langer, M., von Deimling, T. S., Westermann, S., Rolph, R., Rutte, R., Antonova, S., Rachold, V., Schultz, M., Oehme, A., and Grosse, G.: Thawing permafrost poses environmental threat to thousands of sites with legacy industrial contamination, Nature Communications, 14, https://doi.org/10.1038/s41467-023-37276-4, URL http://dx.doi.org/10.1038/s41467-023-37276-4, 2023.

Li, L. and Pomeroy, J. W.: Estimates of Threshold Wind Speeds for Snow Transport Using Meteorological Data, Journal of Applied Meteorology, 36, 205 – 213, https://doi.org/10.1175/1520-0450(1997)036⟨0205:EOTWSF⟩2.0.CO;2, URL https://journals.ametsoc.org/view/journals/apme/36/3/1520-0450_1997_036_0205_eotwsf_2.0.co_2.xml, 1997.

Marsh, P., Pomeroy, J., Pohl, S., Quinton, W., Onclin, C., Russell, M., Neumann, N., Pietroniro, A., Davison, B., and McCartney, S.: Snowmelt Processes and Runoff at the Arctic Treeline: Ten Years of MAGS Research, pp. 97–123, Springer Berlin Heidelberg, Berlin, Heidelberg, https://doi.org/10.1007/978-3-540-75136-6_6, URL https://doi.org/10.1007/978-3-540-75136-6_6, 2008.

Nadal-Romero, E., Revuelto, J., Errea, P., and López-Moreno, J. I.: The application of terrestrial laser scanner and SfM photogrammetry in measuring erosion and deposition processes in two opposite slopes in a humid badlands area (central Spanish Pyrenees), SOIL, 1, 561–573, https://doi.org/10.5194/soil-1-561-2015, URL https://soil.copernicus.org/articles/1/561/2015/, 2015.

Niittynen, P., Heikkinen, R. K., and Luoto, M.: Snow cover is a neglected driver of Arctic biodiversity loss, Nature Climate Change, 8, 997–1001, https://doi.org/10.1038/s41558-018-0311-x, URL https://tc.copernicus.org/articles/16/87/2022/tc-16-87-2022.pdf, 2018.

Nill, L., Grünberg, I., Ullmann, T., Gessner, M., Boike, J., and Hostert, P.: Arctic shrub expansion revealed by Landsat-derived multitemporal vegetation cover fractions in the Western Canadian Arctic, Remote Sensing of Environment, 281, 113 228, https://doi.org/10.1016/j.rse.2022.113228, 2022.

Painter, T. H., Berisford, D. F., Boardman, J. W., Bormann, K. J., Deems, J. S., Gehrke, F., Hedrick, A., Joyce, M., Laidlaw, R., Marks, D., Mattmann, C., McGurk, B., Ramirez, P., Richardson, M., Skiles, S. M., Seidel, F. C., and Winstral, A.: The Airborne Snow Observatory: Fusion of scanning lidar, imaging spectrometer, and physically-based modeling for mapping snow water equivalent and snow albedo, Remote Sensing of Environment, 184, 139–152, https://doi.org/https://doi.org/10.1016/j.rse.2016.06.018, URL https://www.sciencedirect.com/science/article/pii/S0034425716302577, 2016.

Pan, X., Yang, D., Li, Y., Barr, A., Helgason, W., Hayashi, M., Marsh, P., Pomeroy, J., and Janowicz, R. J.: Bias corrections of precipitation measurements across experimental sites in different ecoclimatic regions of western Canada, The Cryosphere, 10, 2347–2360, https://doi.org/10.5194/tc-10-2347-2016, URL https://tc.copernicus.org/articles/10/2347/2016/, 2016.

Parr, C., Sturm, M., and Larsen, C.: Snowdrift landscape patterns: An Arctic investigation, Water Resources Research, 56, e2020WR027 823, https://doi.org/10.1029/2020WR027823, 2020.

Perma-X Crew: Expedition Report Week 3 - Perma-X Canada 2023, NASA Arctic-Boreal Vulnerability Experiment, URL https://above.nasa.gov/airborne/documents/2023/Expedition%20Report%20Week%203%20-%20Perma-X%20Canada%202023.pdf, accessed: 2024-04-26, 2023.

Pingel, T., Clarke, K., and Mcbride, W.: An Improved Simple Morphological Filter for the Terrain Classification of Airborne LIDAR Data, ISPRS Journal of Photogrammetry and Remote Sensing, 77, 21–30, https://doi.org/10.1016/j.isprsjprs.2012.12.002, 2013.

Pohl, S. and Marsh, P.: Modelling the spatial–temporal variability of spring snowmelt in an arctic catchment, Hydrological Processes: An International Journal, 20, 1773–1792, https://doi.org/doi.org/10.1002/hyp.5955, 2006.

Pomeroy, J., Marsh, P., and Gray, D.: Application of a distributed blowing snow model to the Arctic, Hydrological processes, 11, 1451–1464, https://doi.org/10.1002/(SICI)1099-1085(199709)11:11⟨1451::AID-HYP449⟩3.0.CO;2-Q, 1997.

QGIS Development Team: QGIS Geographic Information System, Open Source Geospatial Foundation, URL http://qgis.osgeo.org, 2023.

Revuelto, J., López-Moreno, J. I., and Alonso-González, E.: Light and shadow in mapping alpine snowpack with unmanned aerial vehicles in the absence of ground control points, Water Resources Research, 57, e2020WR028 980, https://doi.org/10.1029/2020WR028980, URL https://doi.org/10.1029/2020WR028980, 2021.

RIEGL: Long-Range Airborne Laser Scanner for Full Waveform Analysis: RIEGL LMS- Q680i [Datasheet], Riegl LMS, URL http://www.riegl.com/uploads/tx_pxpriegldownloads/10_DataSheet_LMS-Q680i_28-09-2012_01.pdf, 2012.

RIEGL: RIEGL VQ-580 Technical Data, Riegl Laser Measurement Systems GmbH, URL http://www.riegl.com/uploads/tx_pxpriegldownloads/DataSheet_VQ-580_2015-03-23.pdf, accessed: 2023-11-22, 2015.

Rutter, N.: Field snow depth surveys of Trail Valley Creek, unpublished Work, 2023.

Rutter, N., Sandells, M., Derksen, C., Toose, P., Royer, A., Montpetit, B., Langlois, A., Lemmetyinen, J., and Pulliainen, J.: Snow stratigraphic heterogeneity within ground-based passive microwave radiometer footprints: Implications for emission modeling, Journal of Geophysical Research: Earth Surface, 119, 550–565, https://doi.org/10.1002/2013JF003017, 2014.

Rutter, N., Sandells, M. J., Derksen, C., King, J., Toose, P., Wake, L., Watts, T., Essery, R., Roy, A., Royer, A., Marsh, P., Larsen, C., and Sturm, M.: Effect of snow microstructure variability on Ku-band radar snow water equivalent retrievals, The Cryosphere, 13, 3045–3059, https://doi.org/10.5194/tc-13-3045-2019, URL `https://tc.copernicus.org/articles/13/3045/2019/`, 2019.

Schneider von Deimling, T., Lee, H., Ingeman-Nielsen, T., Westermann, S., Romanovsky, V., Lamoureux, S., Walker, D. A., Chadburn, S., Trochim, E., Cai, L., Nitzbon, J., Jacobi, S., and Langer, M.: Consequences of permafrost degradation for Arctic infrastructure – bridging the model gap between regional and engineering scales, The Cryosphere, 15, 2451–2471, https://doi.org/10.5194/tc-15-2451-2021, URL `https://tc.copernicus.org/articles/15/2451/2021/`, 2021.

Schuur, E. A., McGuire, A. D., Schädel, C., Grosse, G., Harden, J. W., Hayes, D. J., Hugelius, G., Koven, C. D., Kuhry, P., Lawrence, D. M., et al.: Climate change and the permafrost carbon feedback, Nature, 520, 171–179, https://doi.org/10.1038/nature14338, URL `http://dx.doi.org/10.1038/nature14338`, 2015.

Shirley, I., Uhlemann, S., Peterson, J., Bennett, K., Hubbard, S. S., and Dafflon, B.: Disentangling the effect of geomorphological features and tall shrubs on snow depth variation in a sub-Arctic watershed using UAV derived products, EGUsphere, 2023, 1–23, https://doi.org/10.5194/egusphere-2023-968, 2023.

Skaugen, T. and Melvold, K.: Modeling the snow depth variability with a high-resolution lidar data set and nonlinear terrain dependency, Water Resources Research, 55, 9689–9704, https://doi.org/10.1029/2019WR025030, 2019.

Sturm, M. and Holmgren, J.: An Automatic Snow Depth Probe for Field Validation Campaigns, Water Resources Research, 54, 9695–9701, https://doi.org/10.1029/2018WR023559, URL `https://agupubs.onlinelibrary.wiley.com/doi/abs/10.1029/2018WR023559`, 2018.

Sturm, M., Holmgren, J., McFadden, J. P., Liston, G. E., Chapin, F. S., and Racine, C. H.: Snow–shrub interactions in Arctic tundra: a hypothesis with climatic implications, Journal of Climate, 14, 336–344, https://doi.org/10.1175/1520-0442(2001)014⟨0336:SSIIAT⟩2.0.CO;2, 2001.

Sturm, M., Taras, B., Liston, G. E., Derksen, C., Jonas, T., and Lea, J.: Estimating snow water equivalent using snow depth data and climate classes, Journal of Hydrometeorology, 11, 1380–1394, https://doi.org/https://doi.org/10.1175/2010JHM1202.1, 2010.

Taylor, P. C., Cai, M., Hu, A., Meehl, J., Washington, W., and Zhang, G. J.: A Decomposition of Feedback Contributions to Polar Warming Amplification, Journal of Climate, 26, 7023–7043, https://doi.org/10.1175/jcli-d-12-00696.1, URL `http://dx.doi.org/10.1175/jcli-d-12-00696.1`, 2013.

Thompson, A., Kelly, R., and Marsh, P.: Spatial variability of snow at Trail Valley Creek, NWT, in: 73rd Eastern Snow Conference, Columbus, Ohio, USA, pp. 101–108, 2016.

Wainwright, H. M., Liljedahl, A. K., Dafflon, B., Ulrich, C., Peterson, J. E., Gusmeroli, A., and Hubbard, S. S.: Mapping snow depth within a tundra ecosystem using multiscale observations and Bayesian methods, The Cryosphere, 11, 857–875, https://doi.org/10.5194/tc-11-857-2017, 2017.

Walker, B.: Field snow depth surveys of Trail Valley Creek, unpublished Work, 2023.

Walker, B., Wilcox, E. J., and Marsh, P.: Accuracy assessment of late winter snow depth mapping for tundra environments using Structure-from-Motion photogrammetry, Arctic Science, 7, 588–604, https://doi.org/10.1139/as-2020-0006, 2020.

Walker, D., Billings, W., De Molenaar, J., et al.: Snow-vegetation interactions in tundra environments, Snow ecology, 266, 324, 2001.

Wang, Wei: Snow Depth Retrieval from Wide Band Radar in Trail Valley Creek, Master's thesis, URL `http://hdl.handle.net/10012/17915`, 2022.

Wilcox, E. J., Keim, D., de Jong, T., Walker, B., Sonnentag, O., Sniderhan, A. E., Mann, P., and Marsh, P.: Tundra shrub expansion may amplify permafrost thaw by advancing snowmelt timing, Arctic Science, 5, 202–217, https://doi.org/10.1139/as-2018-0028, 2019.

Wu, X., Naegeli, K., Premier, V., Marin, C., Ma, D., Wang, J., and Wunderle, S.: Evaluation of snow extent time series derived from Advanced Very High Resolution Radiometer global area coverage data (1982–2018) in the Hindu Kush Himalayas, The Cryosphere, 15, 4261–4279, https://doi.org/10.5194/tc-15-4261-2021, URL `https://tc.copernicus.org/articles/15/4261/2021/`, 2021.

Zhang, T.: Influence of the seasonal snow cover on the ground thermal regime: An overview, Reviews of Geophysics, 43, https://doi.org/10.1029/2004RG000157, 2005.

Zhao, Z., De Frenne, P., Peñuelas, J., Van Meerbeek, K., Fornara, D. A., Peng, Y., Wu, Q., Ni, X., Wu, F., and Yue, K.: Effects of snow cover-induced microclimate warming on soil physicochemical and biotic properties, Geoderma, 423, 115 983, https://doi.org/https://doi.org/10.1016/j.geoderma.2022.115983, URL https://www.sciencedirect.com/science/article/pii/S0016706122002907, 2022.

Appendix

7.1 Weather data

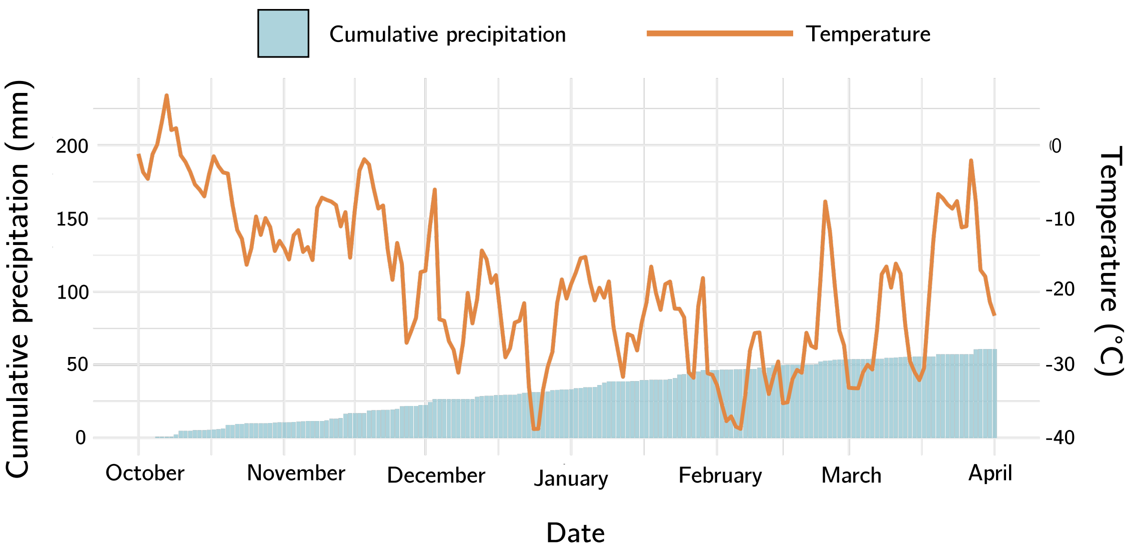

Figure 07.1: Temperature and precipitation: Weather data from the Trail Valley Station within the periods of October 1, 2022 and April 1, 2023 (Government of Canada, Environment and Natural Resources, 2024).

07.1

7.2 Topography distribution

7.2.1 Landforms

Table 7.1: Medians: Landform classes: Comparison among snow depth medians from paired field and LiDAR measurements, and the overall median across the entire area of interest, divided by class

landform	median (m)		
	field	lidar	overall lidar
flat	0.50	0.35	0.29
ridge	0.36	0.11	0.20
shoulder	0.55	0.34	0.25
slope	0.45	0.25	0.32
footslope	0.46	0.26	0.38
valley	–	–	0.44

Table 7.2: Landform descriptive statistics: Summary of the descriptive statistics for snow depth across landforms, including measures of central tendency (mean and median), data spread (standard deviation, variance, range, and interquartile range), and distribution shape (skewness and kurtosis). The count indicates the number of pixel counts within each class.

landform	mean	median	min	max	SD	var	range	IQR	skewness	kurtosis	count
flat	0.31	0.29	-1.23	2.76	0.13	0.02	3.99	0.14	1.80	8.27	33554156
ridge	0.22	0.20	-7.61	3.96	0.13	0.02	11.57	0.13	1.57	43.27	7806187
shoulder	0.28	0.25	-7.05	4.94	0.17	0.03	11.99	0.16	2.99	30.52	24750311
slope	0.38	0.32	-6.84	6.75	0.27	0.07	13.58	0.25	2.99	19.85	39794558
footslope	0.45	0.38	-5.91	8.15	0.33	0.11	14.06	0.28	3.07	18.34	14896840
valley	0.53	0.44	-3.47	6.93	0.38	0.14	10.40	0.36	2.14	9.00	6902639

*SD = Standard Deviation; IQR = Interquartile Range. Units: mean, median, min, max, SD, range, and IQR are in meters (m); var is in square meters (m^2).

Table 7.3: Pairwise LiDAR and field descriptive statistics across landforms: Summary of the descriptive statistics for LiDAR and field snow depth values across landforms, including measures of central tendency (mean and median), data spread (standard deviation, variance, range, and interquartile range), as well as the correlation coefficient (r), and the median of differences (med dif) between both methods. The n indicates the number of paired values.

landform	method	n	mean	med	min	max	SD	var	range	IQR	r	med dif
flat	field	1924	0.53	0.50	0.18	1.38	0.18	0.03	1.19	0.23	0.75	0.14
	lidar		0.39	0.35	0.04	1.62	0.17	0.03	1.58	0.17		
ridge	field	180	0.37	0.36	0.28	0.48	0.05	0.00	0.20	0.08	0.61	0.24
	lidar		0.13	0.11	0.01	0.30	0.06	0.00	0.29	0.10		
shoulder	field	298	0.60	0.55	0.24	1.09	0.21	0.04	0.84	0.34	0.83	0.20
	lidar		0.38	0.34	-0.01	0.96	0.19	0.04	0.97	0.27		
slope	field	1125	0.49	0.45	0.22	1.00	0.15	0.02	0.78	0.15	0.71	0.21
	lidar		0.28	0.25	0.02	0.90	0.15	0.02	0.87	0.20		
footslope	field	437	0.57	0.46	0.28	1.15	0.25	0.06	0.87	0.30	0.89	0.19
	lidar		0.39	0.26	0.06	1.09	0.26	0.07	1.04	0.38		

*SD = Standard Deviation; IQR = Interquartile Range; Units: mean, med, min, max, SD, range, IQR, and med dif are in meters (m); var is in square meters (m^2).

7.2.2 Slope and aspect

Table 7.4: Slope descriptive statistics: Summary of the descriptive statistics for snow depth across slope ranges, regardless of aspect, including measures of central tendency (mean and median), data spread (standard deviation, variance, range, and interquartile range), and distribution shape (skewness and kurtosis). The count indicates the number of pixel counts within each class.

slope	mean	median	min	max	SD	var	range	IQR	skewness	kurtosis	count
flat	0.293	0.275	-4.99	7.71	0.132	0.0175	12.70	0.143	1.92	12.50	21461687
slight	0.314	0.286	-5.64	6.99	0.160	0.0255	12.60	0.167	2.07	11.00	46435802
moderate	0.342	0.301	-6.97	7.27	0.197	0.0387	14.20	0.215	1.92	9.13	27595997
steep	0.447	0.358	-7.61	8.15	0.374	0.140	15.80	0.342	2.49	12.30	32210308

*SD = Standard Deviation; IQR = Interquartile Range. Units: mean, median, min, max, SD, range, and IQR are in meters (m); var is in square meters (m^2).

Table 7.5: Pairwise LiDAR and field descriptive statistics across slope ranges: Summary of the descriptive statistics for LiDAR and field snow depth values across slope classes, including measures of central tendency (mean and median), data spread (standard deviation, variance, range, and interquartile range), as well as the correlation coefficient (r), and the median of differences (med dif) between both methods. The n indicates the number of paired values.

slope	method	n	mean	med	min	max	SD	var	range	IQR	r	med dif
flat	field	1310	0.48	0.45	0.22	1.15	0.15	0.02	0.93	0.18	0.78	0.18
	lidar		0.31	0.29	0.04	1.04	0.16	0.02	1.01	0.19		
slight	field	1951	0.53	0.48	0.18	1.17	0.19	0.04	0.99	0.24	0.80	0.17
	lidar		0.36	0.32	0.02	1.10	0.19	0.03	1.08	0.22		
moderate	field	568	0.54	0.48	0.27	1.38	0.19	0.04	1.11	0.20	0.82	0.19
	lidar		0.35	0.30	-0.01	1.62	0.22	0.05	1.63	0.26		
steep	field	135	0.70	0.74	0.38	1.30	0.21	0.04	0.93	0.37	0.62	0.29
	lidar		0.45	0.39	0.06	1.57	0.25	0.06	1.51	0.27		

*SD = Standard Deviation; IQR = Interquartile Range; Units: mean, med, min, max, SD, range, IQR, and med dif are in meters (m); var is in square meters (m^2).

Table 7.6: Slope and aspect descriptive statistics: Summary of the descriptive statistics for snow depth across slope ranges and aspects, including measures of central tendency (mean and median), data spread (standard deviation, variance, range, and interquartile range), and distribution shape (skewness and kurtosis). The count indicates the number of pixel counts within each class.

slope	aspect	mean	median	min	max	SD	var	range	IQR	skewness	kurtosis	count
flat	north	0.29	0.27	-1.62	7.35	0.14	0.02	8.97	0.15	1.96	15.96	2675649
flat	northeast	0.30	0.28	-3.67	6.37	0.13	0.02	10.05	0.14	1.83	11.30	3308889
flat	east	0.30	0.29	-5.82	5.61	0.13	0.02	11.43	0.14	1.80	12.00	3785799
flat	southeast	0.30	0.28	-1.68	6.27	0.13	0.02	7.96	0.14	1.93	12.51	3223386
flat	south	0.29	0.27	-4.99	5.44	0.13	0.02	10.43	0.14	1.95	12.53	2452201
flat	southwest	0.28	0.26	-1.18	4.74	0.13	0.02	5.92	0.14	2.03	10.88	1979601
flat	west	0.28	0.26	-1.63	5.73	0.13	0.02	7.36	0.14	2.01	11.13	1878822
flat	northwest	0.28	0.26	-3.07	7.71	0.13	0.02	10.78	0.14	2.05	17.30	2157819
slight	north	0.30	0.27	-4.31	6.10	0.16	0.03	10.41	0.16	2.23	11.61	4936100
slight	northeast	0.33	0.31	-3.53	6.04	0.16	0.03	9.57	0.17	1.94	9.60	6443899
slight	east	0.36	0.33	-4.21	6.99	0.17	0.03	11.20	0.18	1.94	10.78	8356744
slight	southeast	0.34	0.32	-2.68	6.56	0.16	0.03	9.25	0.17	1.99	10.52	7372183
slight	south	0.31	0.28	-4.67	6.81	0.15	0.02	11.48	0.15	2.17	12.92	5883045
slight	southwest	0.28	0.25	-3.33	4.88	0.15	0.02	8.21	0.14	2.44	13.42	4533084
slight	west	0.26	0.24	-5.64	5.77	0.14	0.02	11.40	0.13	2.61	16.93	4105288
slight	northwest	0.27	0.24	-3.72	6.94	0.15	0.02	10.66	0.14	2.55	14.11	4805725
moderate	north	0.29	0.26	-3.80	7.27	0.17	0.03	11.07	0.18	2.42	16.31	3132612
moderate	northeast	0.38	0.35	-3.60	4.02	0.19	0.04	7.62	0.21	1.72	7.81	3597947
moderate	east	0.44	0.40	-3.77	6.70	0.22	0.05	10.47	0.25	1.64	7.06	4435700
moderate	southeast	0.42	0.38	-3.55	7.08	0.21	0.04	10.63	0.22	1.87	8.76	4101906
moderate	south	0.34	0.31	-5.30	5.67	0.17	0.03	10.97	0.18	2.07	12.31	3728876
moderate	southwest	0.28	0.25	-4.31	5.27	0.15	0.02	9.58	0.14	2.55	14.70	3053727
moderate	west	0.24	0.22	-6.97	6.56	0.15	0.02	13.54	0.13	2.91	23.38	2619229
moderate	northwest	0.25	0.22	-5.64	6.02	0.16	0.03	11.65	0.14	2.85	19.13	2926082
steep	north	0.39	0.31	-7.23	6.60	0.32	0.10	13.84	0.28	2.25	11.62	4901112
steep	northeast	0.52	0.44	-6.69	6.75	0.37	0.13	13.44	0.35	2.08	9.34	4298445
steep	east	0.63	0.53	-7.56	6.48	0.45	0.20	14.04	0.43	2.15	8.53	4684279
steep	southeast	0.61	0.49	-6.26	7.18	0.45	0.21	13.43	0.39	2.54	10.61	4289126
steep	south	0.44	0.37	-6.35	6.93	0.33	0.11	13.28	0.28	2.92	16.84	3924587
steep	southwest	0.31	0.26	-7.05	5.55	0.24	0.06	12.60	0.21	1.97	15.15	3173020
steep	west	0.28	0.23	-7.61	8.15	0.23	0.05	15.76	0.20	1.97	16.13	2997329
steep	northwest	0.30	0.24	-6.60	7.66	0.27	0.07	14.26	0.23	2.30	13.37	3942480

*SD = Standard Deviation; IQR = Interquartile Range. Units: mean, median, min, max, SD, range, and IQR are in meters (m); var is in square meters (m^2).

Table 7.7: Pairwise LiDAR and field descriptive statistics across flat slopes: Summary of the descriptive statistics for LiDAR and field snow depth values across flat slopes and their related aspects, including measures of central tendency (mean and median), data spread (standard deviation, variance, range, and interquartile range), as well as the correlation coefficient (r), and the median of differences (med dif) between both methods. The n indicates the number of paired values.

slope	aspect	method	n	mean	med	min	max	SD	var	range	IQR	r	med dif
flat	north	field	124	0.54	0.54	0.31	0.83	0.12	0.02	0.52	0.17	0.59	0.17
		lidar		0.36	0.35	0.13	0.80	0.12	0.01	0.67	0.10		
flat	northeast	field	183	0.52	0.51	0.25	0.88	0.13	0.02	0.63	0.17	0.66	0.17
		lidar		0.35	0.33	0.06	0.75	0.14	0.02	0.69	0.16		
flat	east	field	243	0.46	0.42	0.25	1.15	0.15	0.02	0.90	0.11	0.80	0.21
		lidar		0.28	0.22	0.04	0.95	0.16	0.03	0.92	0.19		
flat	southeast	field	219	0.47	0.42	0.24	1.14	0.17	0.03	0.91	0.15	0.84	0.17
		lidar		0.31	0.27	0.09	1.04	0.18	0.03	0.95	0.23		
flat	south	field	181	0.44	0.40	0.22	1.13	0.17	0.03	0.91	0.15	0.89	0.17
		lidar		0.28	0.24	0.07	0.96	0.17	0.03	0.90	0.20		
flat	southwest	field	123	0.48	0.45	0.23	1.04	0.14	0.02	0.81	0.17	0.82	0.17
		lidar		0.30	0.29	0.06	0.85	0.14	0.02	0.79	0.18		
flat	west	field	121	0.50	0.48	0.23	0.91	0.13	0.02	0.69	0.16	0.66	0.19
		lidar		0.31	0.29	0.09	0.79	0.13	0.02	0.70	0.12		
flat	northwest	field	116	0.51	0.50	0.31	0.89	0.12	0.01	0.58	0.13	0.64	0.17
		lidar		0.34	0.35	0.10	0.70	0.12	0.01	0.60	0.14		

*SD = Standard Deviation; IQR = Interquartile Range; Units: mean, med, min, max, SD, range, IQR, and med dif are in meters (m); var is in square meters (m^2).

Table 7.8: Pairwise LiDAR and field descriptive statistics across slight slopes: Summary of the descriptive statistics for LiDAR and field snow depth values across slight slopes and their related aspects, including measures of central tendency (mean and median), data spread (standard deviation, variance, range, and interquartile range), as well as the correlation coefficient (r), and the median of differences (med dif) between both methods. The n indicates the number of paired values.

slope	aspect	method	n	mean	med	min	max	SD	var	range	IQR	r	med dif
slight	north	field	99	0.53	0.52	0.31	0.80	0.13	0.02	0.49	0.19	0.56	0.17
		lidar		0.35	0.34	0.15	0.76	0.11	0.01	0.62	0.13		
slight	northeast	field	299	0.63	0.60	0.28	1.13	0.20	0.04	0.85	0.24	0.83	0.21
		lidar		0.42	0.40	0.02	1.10	0.21	0.05	1.08	0.28		
slight	east	field	620	0.55	0.47	0.26	1.17	0.21	0.04	0.91	0.26	0.82	0.17
		lidar		0.38	0.35	0.05	1.09	0.19	0.04	1.05	0.22		
slight	southeast	field	440	0.46	0.41	0.20	1.06	0.20	0.04	0.87	0.23	0.82	0.10
		lidar		0.36	0.31	0.06	0.97	0.17	0.03	0.91	0.18		
slight	south	field	225	0.50	0.46	0.18	1.08	0.17	0.03	0.90	0.16	0.82	0.18
		lidar		0.32	0.27	0.02	1.06	0.19	0.04	1.03	0.19		
slight	southwest	field	131	0.47	0.44	0.23	1.09	0.15	0.02	0.86	0.14	0.75	0.23
		lidar		0.25	0.20	0.07	0.95	0.16	0.03	0.88	0.10		
slight	west	field	84	0.52	0.51	0.32	0.96	0.13	0.02	0.64	0.14	0.62	0.20
		lidar		0.31	0.27	0.11	0.60	0.13	0.02	0.50	0.18		
slight	northwest	field	53	0.51	0.50	0.34	0.81	0.12	0.01	0.47	0.11	0.57	0.17
		lidar		0.34	0.32	0.14	0.69	0.11	0.01	0.55	0.13		

*SD = Standard Deviation; IQR = Interquartile Range; Units: mean, med, min, max, SD, range, IQR, and med dif are in meters (m); var is in square meters (m^2).

Table 7.9: Pairwise LiDAR and field descriptive statistics across moderate slopes: Summary of the descriptive statistics for LiDAR and field snow depth values across moderate slopes and their related aspects, including measures of central tendency (mean and median), data spread (standard deviation, variance, range, and interquartile range), as well as the correlation coefficient (r), and the median of differences (med dif) between both methods. The n indicates the number of paired values.

slope	aspect	method	n	mean	med	min	max	SD	var	range	IQR	r	med dif
moderate	north	field	4	0.45	0.44	0.43	0.49	0.03	0.00	0.06	0.02	0.90	0.16
		lidar		0.29	0.28	0.24	0.34	0.04	0.00	0.10	0.05		
moderate	northeast	field	99	0.62	0.57	0.34	0.94	0.15	0.02	0.61	0.23	0.54	0.12
		lidar		0.51	0.48	0.15	1.01	0.19	0.04	0.87	0.23		
moderate	east	field	108	0.65	0.71	0.32	1.37	0.23	0.05	1.05	0.34	0.92	0.26
		lidar		0.41	0.42	-0.01	1.62	0.28	0.08	1.63	0.30		
moderate	southeast	field	116	0.52	0.45	0.27	1.38	0.23	0.05	1.11	0.23	0.90	0.13
		lidar		0.38	0.32	0.09	1.47	0.24	0.06	1.38	0.25		
moderate	south	field	191	0.45	0.44	0.29	0.97	0.10	0.01	0.69	0.07	0.67	0.21
		lidar		0.25	0.22	0.05	0.91	0.12	0.02	0.86	0.14		
moderate	southwest	field	34	0.54	0.53	0.31	0.99	0.12	0.01	0.68	0.08	0.66	0.30
		lidar		0.26	0.22	0.08	0.75	0.16	0.02	0.66	0.14		
moderate	west	field	16	0.47	0.45	0.36	0.69	0.07	0.01	0.33	0.08	0.58	0.26
		lidar		0.22	0.20	0.10	0.49	0.09	0.01	0.38	0.07		

*SD = Standard Deviation; IQR = Interquartile Range; Units: mean, med, min, max, SD, range, IQR, and med dif are in meters (m); var is in square meters (m^2).

Table 7.10: Pairwise LiDAR and field descriptive statistics across steep slopes: Summary of the descriptive statistics for LiDAR and field snow depth values across steep slopes and their related aspects, including measures of central tendency (mean and median), data spread (standard deviation, variance, range, and interquartile range), as well as the correlation coefficient (r), and the median of differences (med dif) between both methods. The n indicates the number of paired values.

slope	aspect	method	n	mean	med	min	max	SD	var	range	IQR	r	med dif
steep	north	field	6	0.43	0.44	0.38	0.46	0.03	0.00	0.08	0.03	-0.94	-0.14
		lidar		0.60	0.57	0.47	0.77	0.11	0.01	0.30	0.12		
steep	northeast	field	21	0.81	0.86	0.42	1.30	0.30	0.09	0.88	0.48	0.65	0.11
		lidar		0.77	0.73	0.35	1.57	0.33	0.11	1.22	0.22		
steep	east	field	16	0.72	0.77	0.39	0.93	0.21	0.04	0.54	0.31	0.86	0.30
		lidar		0.43	0.38	0.07	0.95	0.28	0.08	0.88	0.32		
steep	southeast	field	65	0.79	0.78	0.53	1.00	0.11	0.01	0.48	0.13	0.62	0.37
		lidar		0.42	0.39	0.11	0.75	0.13	0.02	0.64	0.14		
steep	south	field	20	0.42	0.42	0.39	0.49	0.02	0.00	0.09	0.03	0.44	0.22
		lidar		0.20	0.20	0.06	0.32	0.07	0.00	0.25	0.09		
steep	southwest	field	6	0.64	0.64	0.54	0.72	0.08	0.01	0.18	0.11	0.94	0.26
		lidar		0.40	0.38	0.19	0.60	0.16	0.02	0.40	0.21		
steep	west	field	1	0.77	0.77	0.77	0.77			0.00	0.00		0.24
		lidar		0.53	0.53	0.53	0.53			0.00	0.00		

*SD = Standard Deviation; IQR = Interquartile Range; Units: mean, med, min, max, SD, range, IQR, and med dif are in meters (m); var is in square meters (m^2).

7.3 Vegetation distribution

7.3.1 Vegetation heights

Table 7.11: Medians: Vegetation height classes: Comparison among snow depth medians from paired field and LiDAR measurements, and the overall median across the entire area of interest, divided by class

Vegetation height	median (m)		
	field	lidar	overall lidar
under 0.1 m	0.46	0.33	0.29
0.1 to 0.5 m	0.46	0.29	0.29
0.5 to 1.5 m	0.94	0.67	0.50
over 1.5 m	0.73	0.43	0.54

Table 7.12: Vegetation height descriptive statistics: Summary of the descriptive statistics for snow depth across vegetation heights, including measures of central tendency (mean and median), data spread (standard deviation, variance, range, and interquartile range), and distribution shape (skewness and kurtosis). The count indicates the number of pixel counts within each class.

vegetation height	mean	median	min	max	SD	var	range	IQR	skewness	kurtosis	count
under 0.1 m	0.32	0.29	-4.77	5.84	0.19	0.03	10.61	0.17	3.32	27.73	64062039
0.1 to 0.5 m	0.34	0.29	-6.97	5.85	0.24	0.06	12.83	0.21	3.45	25.20	54622460
0.5 to 1.5 m	0.58	0.50	-7.05	7.18	0.40	0.16	14.23	0.38	1.88	9.03	6574330
over 1.5 m	0.63	0.54	-7.61	8.15	0.45	0.20	15.76	0.43	1.48	9.70	2445862

*SD = Standard Deviation; IQR = Interquartile Range. Units: mean, median, min, max, SD, range, and IQR are in meters (m); var is in square meters (m^2).

Table 7.13: Pairwise LiDAR and field descriptive statistics across vegetation classes: Summary of the descriptive statistics for LiDAR and field snow depth values across vegetation height ranges, including measures of central tendency (mean and median), data spread (standard deviation, variance, range, and interquartile range), as well as the correlation coefficient (r), and the median of differences (med dif) between both methods. The n indicates the number of paired values.

Vegetation	method	n	mean	med	min	max	SD	var	range	IQR	r	med dif
under 0.1 m	field	1402	0.50	0.46	0.23	1.37	0.15	0.02	1.14	0.19	0.74	0.16
	lidar		0.34	0.33	0.02	1.58	0.16	0.03	1.56	0.19		
0.1 to 0.5 m	field	2274	0.50	0.46	0.18	1.38	0.16	0.03	1.19	0.18	0.75	0.19
	lidar		0.32	0.29	-0.01	1.62	0.17	0.03	1.63	0.20		
0.5 to 1.5 m	field	198	0.91	0.94	0.43	1.32	0.17	0.03	0.89	0.27	0.81	0.23
	lidar		0.66	0.67	0.11	1.18	0.22	0.05	1.07	0.37		
over 1.5 m	field	90	0.71	0.73	0.38	0.96	0.11	0.01	0.58	0.13	0.38	0.29
	lidar		0.43	0.43	0.12	0.77	0.14	0.02	0.65	0.15		

*SD = Standard Deviation; IQR = Interquartile Range; Units: mean, med, min, max, SD, range, IQR, and med dif are in meters (m); var is in square meters (m^2).

7.3.2 Vegetation classes

Table 7.14: Medians: Vegetation classes: Comparison among snow depth medians from paired field and LiDAR measurements, and the overall median across the entire area of interest, divided by class

Vegetation	median (m)		
	field	lidar	overall lidar
river	0.75	0.67	0.64
baresoil	0.72	0.47	0.43
polygon wet	0.56	0.32	0.41
polygon dry	0.46	0.32	0.26
lichen	0.46	0.34	0.33
moss	0.51	0.32	0.30
dry hummock	0.45	0.33	0.29
tussock	0.39	0.19	0.25
dwarf shrub	0.47	0.23	0.27
single shrub	0.76	0.51	0.49
riparian shrub	0.98	0.76	0.49
tree	0.73	0.42	0.46

Table 7.15: Vegetation classes descriptive statistics: Summary of the descriptive statistics for snow depth across vegetation classes, including measures of central tendency (mean and median), data spread (standard deviation, variance, range, and interquartile range), and distribution shape (skewness and kurtosis). The count indicates the number of pixel counts within each class.

vegetation	mean	median	min	max	SD	var	range	IQR	skewness	kurtosis	count
river	0.71	0.64	-4.67	5.18	0.41	0.17	9.85	0.49	0.87	3.81	437135
baresoil	0.55	0.43	-7.05	7.66	0.51	0.26	14.71	0.48	2.20	8.17	1889452
polygon wet	0.44	0.41	-2.33	5.13	0.23	0.05	7.46	0.23	1.80	11.37	436474
polygon dry	0.27	0.26	-1.72	2.34	0.10	0.01	4.06	0.12	0.92	4.77	5302022
lichen	0.38	0.33	-2.63	6.83	0.24	0.06	9.46	0.24	2.38	13.28	13413426
moss	0.32	0.30	-1.63	4.84	0.15	0.02	6.46	0.17	1.73	9.53	14274391
dry hummock	0.32	0.29	-2.01	4.35	0.15	0.02	6.36	0.16	1.85	8.49	36253638
tussock	0.27	0.25	-0.73	3.66	0.12	0.01	4.39	0.13	1.78	11.59	9479275
dwarf shrub	0.32	0.27	-5.50	7.45	0.23	0.05	12.95	0.21	3.09	20.36	34153688
single shrub	0.61	0.49	-7.56	8.15	0.46	0.21	15.71	0.38	2.33	9.38	6596688
riparian shrub	0.55	0.49	-5.72	5.91	0.35	0.12	11.63	0.39	1.19	5.81	4531475
tree	0.51	0.46	-7.61	5.55	0.41	0.17	13.16	0.33	0.43	13.59	937027

*SD = Standard Deviation; IQR = Interquartile Range. Units: mean, median, min, max, SD, range, and IQR are in meters (m); var is in square meters (m^2).

Table 7.16: Pairwise LiDAR and field descriptive statistics across vegetation classes: Summary of the descriptive statistics for LiDAR and field snow depth values across vegetation, including measures of central tendency (mean and median), data spread (standard deviation, variance, range, and interquartile range), as well as the correlation coefficient (r), and the median of differences (med dif) between both methods. The n indicates the number of paired values.

Vegetation	method	n	mean	med	min	max	SD	var	range	IQR	r	med dif
river	field	14	0.76	0.75	0.64	1.04	0.10	0.01	0.41	0.07	0.50	0.18
	lidar		0.63	0.67	0.36	0.85	0.13	0.02	0.49	0.13		
baresoil	field	2	0.72	0.72	0.50	0.94	0.31	0.10	0.44	0.22	1.00	0.25
	lidar		0.47	0.47	0.20	0.73	0.37	0.14	0.52	0.26		
polygon wet	field	5	0.56	0.56	0.45	0.70	0.09	0.01	0.25	0.02	0.31	0.23
	lidar		0.40	0.32	0.28	0.60	0.15	0.02	0.32	0.24		
polygon dry	field	356	0.47	0.46	0.18	0.87	0.09	0.01	0.68	0.11	0.38	0.15
	lidar		0.32	0.32	0.04	0.62	0.09	0.01	0.58	0.11		
lichen	field	195	0.49	0.46	0.23	1.30	0.15	0.02	1.08	0.10	0.74	0.12
	lidar		0.38	0.34	0.08	1.57	0.20	0.04	1.49	0.17		
moss	field	910	0.53	0.51	0.23	1.11	0.15	0.02	0.88	0.23	0.75	0.19
	lidar		0.34	0.32	0.06	0.85	0.16	0.03	0.79	0.23		
dry hummock	field	935	0.47	0.45	0.20	1.38	0.16	0.03	1.18	0.20	0.77	0.12
	lidar		0.36	0.33	0.06	1.62	0.16	0.03	1.57	0.15		
tussock	field	429	0.39	0.39	0.22	1.06	0.09	0.01	0.84	0.08	0.70	0.19
	lidar		0.22	0.19	0.02	0.86	0.11	0.01	0.84	0.10		
dwarf shrub	field	737	0.52	0.47	0.27	1.30	0.16	0.03	1.03	0.15	0.82	0.25
	lidar		0.28	0.23	-0.01	1.16	0.18	0.03	1.17	0.20		
single shrub	field	218	0.79	0.76	0.25	1.32	0.17	0.03	1.07	0.21	0.76	0.24
	lidar		0.54	0.51	0.07	1.18	0.20	0.04	1.11	0.26		
riparian shrub	field	108	0.98	0.98	0.59	1.15	0.10	0.01	0.56	0.16	0.63	0.22
	lidar		0.75	0.76	0.28	1.09	0.18	0.03	0.82	0.26		
tree	field	55	0.70	0.73	0.38	0.99	0.10	0.01	0.61	0.12	0.19	0.30
	lidar		0.41	0.42	0.14	0.65	0.13	0.02	0.51	0.14		

*SD = Standard Deviation; IQR = Interquartile Range; Units: mean, med, min, max, SD, range, IQR, and med dif are in meters (m); var is in square meters (m^2).

Erklärung

Ich erkläre, dass ich die vorliegende Arbeit oder Teile davon nicht für andere Prüfungs- und Studienleistungen eingereicht, selbständig und nur unter Verwendung der angegebenen Literatur und Hilfsmittel angefertigt habe. Sämtliche fremde Quellen inklusive Internetquellen, Grafiken, Tabellen und Bilder, die ich unverändert oder abgewandelt wiedergegeben habe, habe ich als solche kenntlich gemacht. Mir ist bekannt, dass Verstöße gegen diese Grundsätze als Täuschungsversuch bzw. Täuschung geahndet werden.

Daniela Hollenbach Borges

Berlin, den 6. November 2023